NEUROSCIENCE

Context-dependent plasticity of adult-born neurons regulated by cortical feedback

An Wu[1,2]*†, Bin Yu[1,2,3]*, Qiyu Chen[1,2], Gillian A. Matthews[4], Chen Lu[1,2], Evan Campbell[1], Kay M. Tye[4], Takaki Komiyama[1,2]†

In a complex and dynamic environment, the brain flexibly adjusts its circuits to preferentially process behaviorally relevant information. Here, we investigated how the olfactory bulb copes with this demand by examining the plasticity of adult-born granule cells (abGCs). We found that learning of olfactory discrimination elevates odor responses of young abGCs and increases their apical dendritic spines. This plasticity did not occur in abGCs during passive odor experience nor in resident granule cells (rGCs) during learning. Furthermore, we found that feedback projections from the piriform cortex show elevated activity during learning, and activating piriform feedback elicited stronger excitatory postsynaptic currents in abGCs than rGCs. Inactivation of piriform feedback blocked abGC plasticity during learning, and activation of piriform feedback during passive experience induced learning-like plasticity of abGCs. Our work describes a neural circuit mechanism that uses adult neurogenesis to update a sensory circuit to flexibly adapt to new behavioral demands.

INTRODUCTION

The brain is constantly bombarded by a rich repertoire of sensory inputs. Of these inputs, only a small subset is behaviorally meaningful. Therefore, it is crucial for animals to efficiently allocate the limited resources of their brain to process behaviorally relevant stimuli. To achieve this goal, the brain has evolved to use experience-dependent plastic mechanisms to refine neural circuits in sensory systems. A marked example is found in the developmental critical period of visual system. A cat reared viewing only unidirectional stripes does not develop the ability to represent and perceive visual stimuli orthogonal to the experienced stripes (1). Not all such changes are limited to developmental periods, however, and even in adulthood, sensory systems of animals undergo constant modifications to cope with the changing environment.

In olfaction, the incoming sensory information from the nose first arrives at the olfactory bulb. Here, the axons of olfactory sensory neurons expressing the same odorant receptor converge and excite mitral/tufted cells, the output neurons of the bulb that send their axons to higher brain centers including the piriform cortex (Fig. 1A) (2). Despite this simple excitatory feedforward pathway, the olfactory bulb does not function as a passive relay of olfactory information to higher brain areas. Instead, the olfactory bulb actively processes information in an experience-dependent manner (3). For instance, it is established that the degree of pattern separation by the mitral cell population is modulated by experience and that learning to discriminate similar odorants enhances pattern separation for the learned odors (4–6). This modulation of mitral cell activity is mediated by extensive local inhibitory circuits within the olfactory bulb. The vast majority of bulbar inhibitory neurons are granule cells

(GCs), whose apical dendrites form dendrodendritic synapses with mitral/tufted cells (2). The lateral inhibition provided by GCs is believed to be critical for mitral cell pattern separation (7). GCs are also the major target of various feedback projections from the central brain (2). In particular, glutamatergic feedback from the piriform cortex that arrives at the perisomatic area and/or basal dendrites of GCs is among the most abundant feedback. This piriform feedback shows odor-tuned responses and contributes to the modulation of mitral cell activity by GCs (Fig. 1B) (8–10).

The olfactory bulb is one of the two regions in the rodent brain where substantial numbers of new neurons are added to the existing circuitry throughout life. Adult neurogenesis in the subventricular zone in the central brain generates thousands of new neurons every day, and these new neurons migrate through the rostral migratory stream (RMS) and arrive at the olfactory bulb a few days later (11). Approximately 95% of newly generated neurons differentiate into GCs (12). After their arrival in the bulb, adult-born GCs (abGCs) undergo a highly plastic period of ~8 weeks before becoming fully integrated into the local circuit. Morphologically, abGCs gradually extend both their basal and apical dendrites (13–15). Sensory experience and learning can modulate the integration of young abGCs, suggesting that their maturation is activity-dependent (14, 16–21). Furthermore, recent in vivo experiments revealed that the odor response properties of young abGCs evolve in an experience- and learning-dependent manner during maturation (22–24). Thus, adult neurogenesis provides the olfactory bulb circuit with additional flexibility to adapt to the dynamic environment. Consistent with this notion, ablation of adult neurogenesis in the olfactory bulb can lead to impairment in olfactory behaviors (25, 26). In particular, we recently showed that genetic ablation of young adult-born neurons impairs mitral cell pattern separation and behavioral performance in a difficult discrimination task but not an easy discrimination task (27). Furthermore, activating adult-born neurons or genetically enhancing adult neurogenesis can facilitate difficult odor discrimination without affecting easy discrimination (28, 29).

Together, it appears that adult neurogenesis critically contributes to olfactory perceptual learning to discriminate similar odorants. Studies using postmortem histology have reported that abGCs

[1]Neurobiology Section, and Center for Neural Circuits and Behavior, University of California San Diego, La Jolla, CA 92093, USA. [2]Department of Neurosciences, and Halıcıoğlu Data Science Institute, University of California San Diego, La Jolla, CA 92093, USA. [3]Department of Electrical and Computer Engineering, University of California San Diego, La Jolla, CA 92093, USA. [4]Salk Institute for Biological Studies, La Jolla, CA 92037, USA.
*These authors contributed equally to this work.
†Corresponding author. Email: tkomiyama@ucsd.edu (T.K.); anwu.ucsd@gmail.com (A.W.)
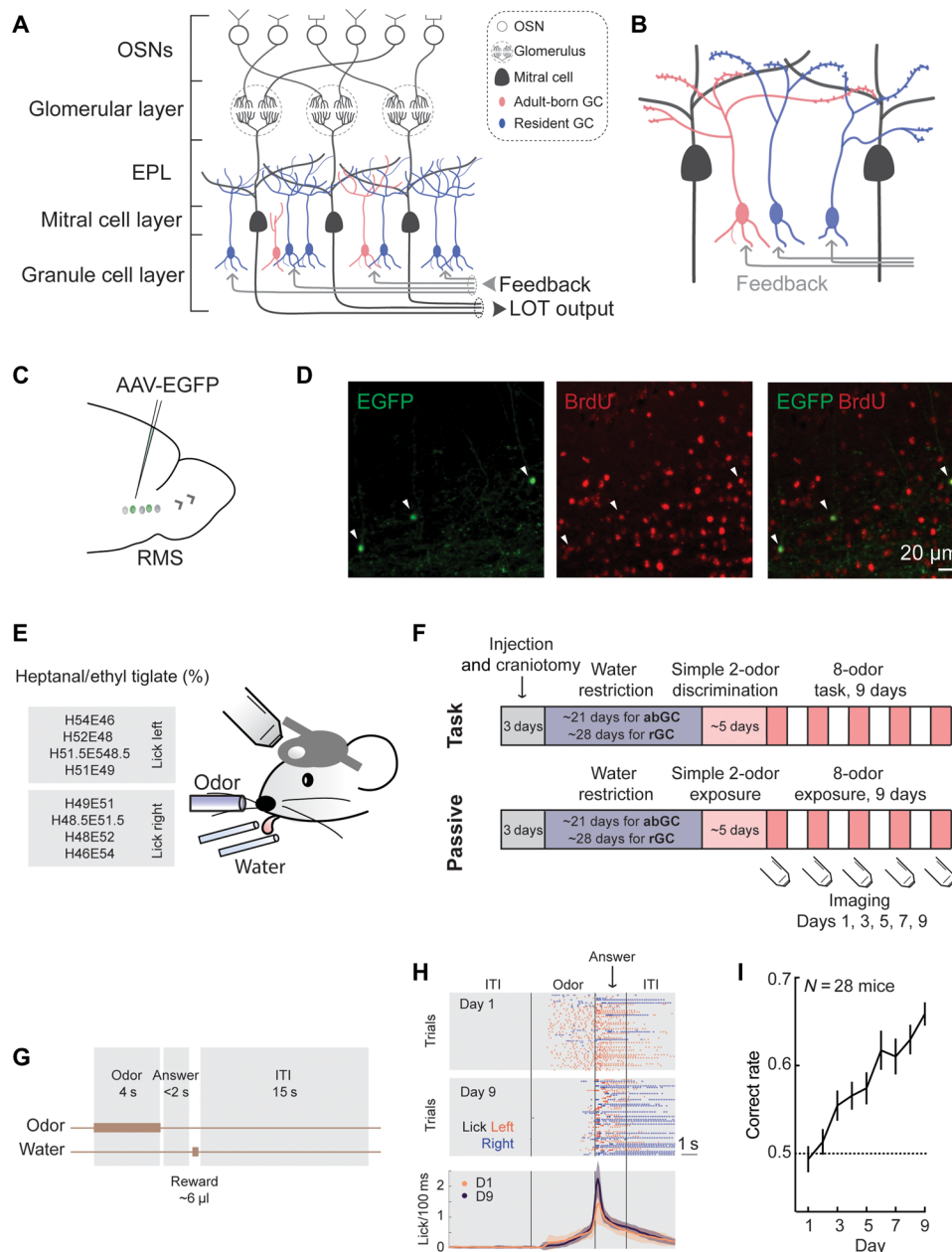
Fig. 1. Schematic of the olfactory bulb circuit and experimental setup. (**A** and **B**) Schematics of the olfactory bulb circuit. GCs receive feedback inputs in their basal dendrites and/or perisomatic region and form reciprocal synapses with mitral cells in their apical dendrites. GC apical dendrites can mediate lateral inhibition across mitral cells. OSN, olfactory sensory neuron; EPL, external plexiform layer; GC, granule cell; LOT, lateral olfactory tract. (**C**) Schematic of the viral injection in the RMS to label abGCs with EGFP. (**D**) BrdU staining confirms that our RMS injection labels young abGCs. Arrowheads, abGCs double-labeled with BrdU and EGFP. (**E**) Schematic of mice performing the two alternative choices, 8-odor discrimination task under microscope. (**F**) Timeline of task and passive experience. Imaging was performed on D1, D3, D5, D7, and D9. (**G**) Schematic of trial structure. (**H**) Top: Lick patterns in all trials on D1 and D9 in one example mouse. Each dot represents a lick. Bottom: Trial-averaged lick rate on D1 (orange) and D9 (purple) (abGC-labeled mice, $n = 8$ mice). Mean ± SEM. (**I**) Behavioral correct rate from 28 mice (abGC- and rGC-labeled mice were pooled) over 9 days of learning. Dotted line represents the chance level. Mean ± SEM.

exhibit learning- and experience-induced increases in apical and basal dendritic spines (*18*, *30*). However, in vivo dynamics of abGC plasticity during different behavioral contexts are poorly understood. Furthermore, the circuit mechanisms regulating abGC plasticity are unknown. Here, we took advantage of a difficult discrimination task that requires adult neurogenesis and investigated the structural

and functional plasticity of young abGCs and resident GCs (rGCs) by in vivo longitudinal two-photon imaging. These experiments revealed that young abGCs undergo selective, cell-specific plasticity during learning but not during passive experience of the same odorants. Furthermore, we found that the context specificity of abGC plasticity is instructed by glutamatergic feedback projections from

the piriform cortex to the olfactory bulb. These results reveal a neural circuit mechanism that dynamically updates a sensory circuit to preferentially process behaviorally relevant sensory stimuli.

RESULTS

abGCs show task-induced functional plasticity

To label abGCs in the olfactory bulb, we injected adeno-associated virus (AAV)–CB7-EGFP into the RMS to transfect neuroblasts migrating to the olfactory bulb (Fig. 1C). Immediately after the RMS injection, we placed a chronic imaging window over the olfactory bulb for longitudinal in vivo imaging of abGCs. To confirm that this method selectively labels abGCs, we performed double labeling with 5-bromo-2′-deoxyuridine (BrdU) administered orally for 2 weeks before the AAV injection. This experiment showed that at least 92% of neurons labeled with AAV were recently born abGCs (108 of 117 neurons labeled with AAV were BrdU positive; $n = 2$ mice; Fig. 1D).

We trained water-restricted mice with a difficult olfactory discrimination task under head fixation over 9 days (150 trials per day; Fig. 1E). Before the training with the difficult discrimination task, mice underwent a pretraining period during which mice were familiarized with the task structure with easily discriminable odorants. The experiments were timed such that the training of the difficult discrimination started 28 to 34 days after the RMS injection (Fig. 1F), and so the imaging was done on young abGCs that have been shown to be highly plastic (*31*, *32*). We previously found that learning of this difficult discrimination task selectively requires young abGCs (*27*). In this task, one of the eight similar binary odorant mixtures [heptanal/ethyl tiglate (%): left lick: H54E46, H52E48, H51.5E548.5, H51E49; right lick: H49E51, H48.5E51.5, H48E52, and H46E54] is presented in each trial for 4 s. After the odor period, mice have up to 2 s to lick the left or the right lick port, and correct choices are rewarded with water (~6 µl) (Fig. 1G). Licking during the odor period was allowed and ignored, but in general, mice refrained from licking until close to the answer period (Fig. 1H). Mice improved their performance in this difficult discrimination task over 9 days (Fig. 1I), consistent with our previous report (*27*). The behavioral improvement here which reached ~65% correct rate was worse than what we reported in our previous study (~76%) (*27*). This is likely due to a small change in the training procedure that we made. In the previous study, one of the pairs of the pretraining odors was easily discriminable mixtures of heptanal and ethyl tiglate, the same odors used later for the difficult mixtures. In the current study, we used different odors for pretraining to maximize the effect of learning during the difficult discrimination task.

We performed in vivo two-photon calcium imaging to record the activity of young abGCs expressing genetically encoded calcium indicator protein (GCaMP6f) during the difficult discrimination task (Fig. 2A). The same populations of abGCs were identified and imaged repeatedly at their cell bodies every other day over 9 days [84 abGCs (672 odor-abGC pairs) in eight mice]. A large fraction of the imaged odor-abGC pairs showed either significantly higher (excitatory) or lower (suppressive) activity than baseline during odor periods in at least one of the five imaged sessions (Fig. 2, B and C, and figs. S1A and S2 and see Materials and Methods). If an odor-abGC pair showed excitatory (or suppressive) responses in at least one of the five sessions and did not switch to suppressive (or excitatory) responses in other sessions, they were classified as excitatory (or suppressive,

30 and 17% respectively). Only a small fraction (4%) of odor-abGC pairs switched between excitatory and suppressive responses over the 9 days (the "switch" group). Another small portion (4%) of odor-abGC pairs showed transient excitatory activity at the odor onset followed by suppressive activity, which was categorized as the "onset-transient" group.

We examined the excitatory and suppressive odor-abGC pairs separately. [In this analysis, we included the switch group in both excitatory and suppressive populations. However, the results were unaffected when we removed the switch group (fig. S3, A and B).] We found that excitatory odor-abGC pairs increased their responses during learning (Fig. 2, D and E, and fig. S1B). This increase in responses accompanied an increase in the early responses near the odor onset and a shift toward faster responses (Fig. 2, E and F, and fig. S1C). The fraction of daily excitatory odor-abGC pairs on each day showed only modest and nonsignificant increase (fig. S1D). Instead, the increase in responses was mainly driven by the stronger responses of individual excitatory odor-abGC pairs in later days (fig. S1E). Furthermore, the onset-transient odor-abGC pairs increased their mean activity during the first second of the odor period during learning (fig. S3, C and D). In contrast, the amplitude of responses of suppressive pairs decreased during learning (Fig. 2, D and E, and fig. S1B). Together, odor responses of abGCs shifted toward stronger excitatory responses with learning.

To address whether the excitatory shift in the abGC population response depends on task engagement, we performed a parallel experiment in which a separate group of mice experienced the odors passively [122 abGCs (976 odor-abGC pairs) in six mice]. These "passive" mice were treated, handled, and water-restricted identically to the learning group and experienced the same odors the same number of times, including the pretraining odors, without ever being trained in a task or receiving a reward during odor experience (Fig. 1F). We found marked differences in abGC responses in passive versus task animals. First, we found much higher fractions of responsive odor-abGC pairs in the task condition than in the passive condition (Fig. 2G and fig. S1A), which indicates that task engagement significantly elevates abGC responses. Because of the small number of neurons in each responsive category in the passive condition, we focused on the change of population activity averaged across all odor-abGC pairs over sessions [normalized to activity on day 1 (D1) by subtracting D1 activity from each day]. We found that odor-abGC pairs in task mice show significantly higher increases in odor activity, especially early odor activity (the first second of the odor period), than in passive experience (Fig. 2H). In addition, we performed a decoding analysis to classify odors based on abGC activity and found that abGCs show a higher decoding accuracy in the task condition than the passive condition (fig. S9A). Together, we conclude that task learning specifically enhanced odor activity in abGCs.

We next asked whether the excitatory shift in the population response during learning is specific to abGCs or observed generally in GCs. To address this question, we injected AAVs directly into the GC layer of the olfactory bulb to label the GCs that are already present in the olfactory bulb ("rGCs"; Fig. 2I), a vast majority of which should be developmentally born GCs and mature abGCs. We imaged the activity of these rGCs repeatedly during the 9 days of the difficult discrimination task [218 rGCs (1744 odor-rGC pairs) in six mice; Fig. 2, J and K, and fig. S3E]. The imaging was done 5 to 6 weeks after the AAV injection (Fig. 1F). In contrast to young abGCs, we found that rGCs show an initial attenuation of odor-evoked excitatory
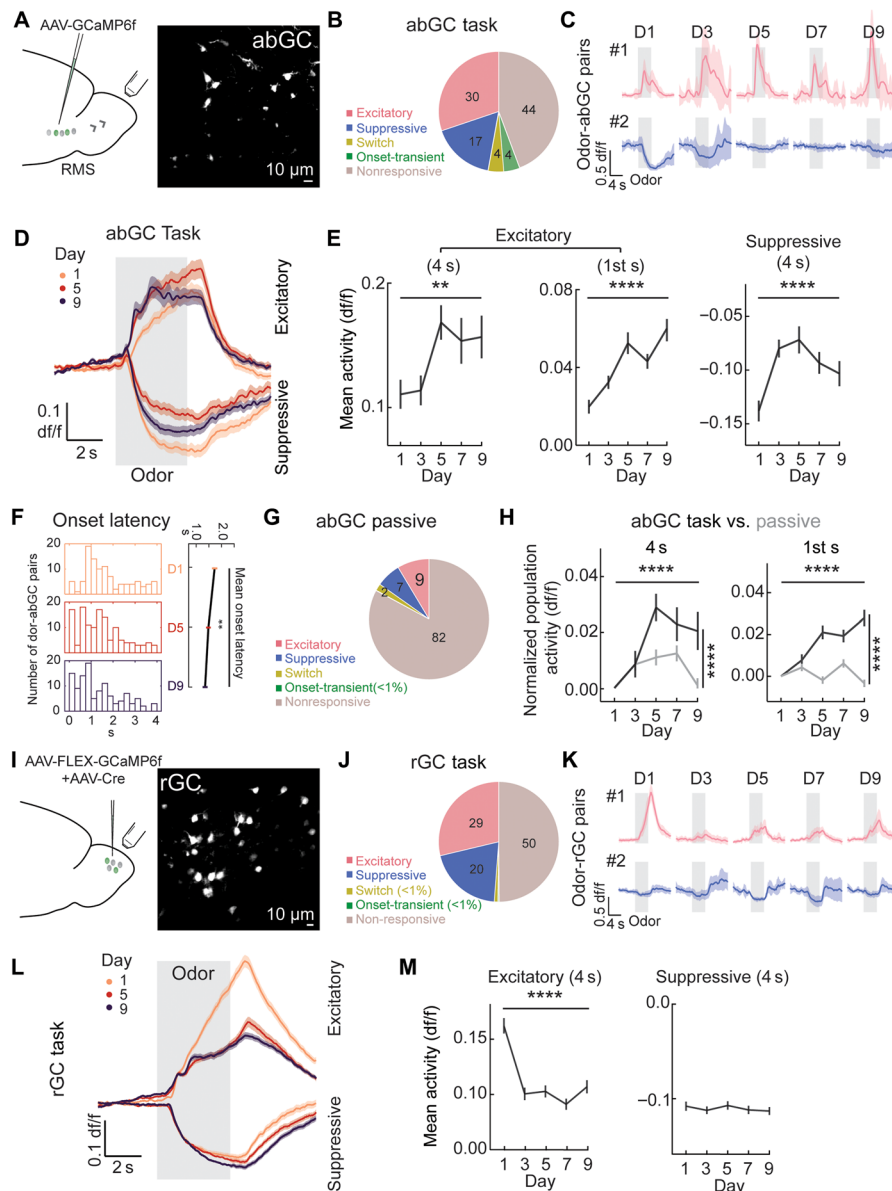
Fig. 2. abGCs show task-induced functional plasticity. (**A**) Left: Schematic of the viral injection to label abGCs with GCaMP6f. Right: Example in vivo two-photon image of GCaMP6f-labeled abGCs. (**B**) Pie chart showing proportions of odor-abGC pairs that are excitatory-only (significant excitatory responses in at least one session and never another response type in another session, red), suppressive-only (blue), switch (yellow), and onset-transient (green) in task. Light brown indicates odor-abGC pairs that were not responsive to odors in all imaging sessions. Numbers in the pie chart are the percentages of different categories. $n = 672$ odor-abGC pairs. (**C**) Example traces of one excitatory (red) and one suppressive (blue) odor-abGC pair over 9 days of task. Gray box, odor period. Mean ± SEM. (**D**) Average population activity of excitatory or suppressive odor-abGC pairs during task on D1 (light orange), 5 (dark orange), and 9 (dark purple), normalized to the baseline (5 s before odor period). Gray box, odor period. Mean ± SEM. (**E**) Mean activity (df/f) during the odor period (left, one-way ANOVA, $P < 0.01$) and the early odor period (the 1st second, middle, one-way ANOVA, $P < 0.0001$) of excitatory odor-abGC pairs ($n = 203$ pairs) or the odor period of suppressive (right, one-way ANOVA, $P < 0.0001$) odor-abGC pairs ($n = 114$ pairs) during task. Mean ± SEM. (**F**) Activity onset latency (see Materials and Methods) histogram (left) and averaged across excitatory odor-abGC pairs (right) during task ($n = 203$ pairs). One-way ANOVA, $P < 0.01$. Mean ± SEM. (**G**) Pie chart showing proportions of odor-abGC pairs that are excitatory-only (red), suppressive-only (blue), switch (yellow), and onset-transient (green) in passive experience. Light brown indicates odor-abGC pairs that were not responsive during 9 days. Chi-square test, p(Task vs. Passive) < 0.0001. Numbers in the pie chart are the percentages of different categories. In total, there are 976 odor-abGC pairs. (**H**) Left: Average population activity of all odor-abGC pairs during the odor period (averaged during the 4-s odor period, normalized by subtracting the D1 values) during task (dark, $n = 672$) and passive experience (light, $n = 976$). Two-way ANOVA, p(group) < 0.0001, p(time) < 0.0001. Right: Average population activity of all odor-abGC pairs during the early odor period (the 1st second, normalized by subtracting the D1 values) during task (dark) and passive experience (light). Two-way ANOVA, p(group) < 0.0001, p(time) < 0.0001. Mean ± SEM. (**I**) Left: Schematic of the viral injection to label rGCs with GCaMP6f. Right: Example in vivo two-photon image of rGCs. (**J**) Pie chart showing proportions of odor-rGC pairs that are excitatory-only (red), suppressive-only (blue), switch (yellow), and onset-transient (green) in task. Light brown indicates odor-rGC pairs that were not responsive during 9 days. Numbers in the pie chart are the percentages of different categories. In total, there are 1744 odor-abGC pairs. (**K**) Example traces of one excitatory (red) and one suppressive (blue) odor-rGC pair over 9 days of task. Mean ± SEM. (**L** and **M**) Similar to (D) and (E) but for rGCs. (**L**) Left: One-way ANOVA, $P < 0.0001$ ($n = 501$ pairs). Right: One-way ANOVA, $P > 0.05$ ($n = 350$ pairs). Mean ± SEM. **, $P < 0.01$, ****, $P < 0.0001$.

responses during the first 3 days and stable suppressive responses, both in the fractions of responsive odor-rGC pairs of each day and mean activity during learning (Fig. 2, L and M, and fig. S3F). We note that the rGCs should include a small portion of younger abGCs; however, this caveat would only underestimate the true differences between young abGCs and mature GCs.

Together, we found that learning selectively recruits young abGCs but not rGCs to increase their excitatory odor responses, suggesting that the balance of bulbar inhibition for learned odors shifts from rGCs to young abGCs during olfactory perceptual learning.

abGCs increase spine density during learning

The primary site of the inhibitory action of GCs is their apical dendrites, which form dendrodendritic synapses with lateral dendrites of mitral cells. The apical dendrites of GCs have been shown to exhibit high degrees of structural plasticity (15). Focusing on the apical dendrites, we examined whether task engagement modulates the structural plasticity of GC dendrites, which could be a basis for the functional plasticity described above. We did this by repeatedly imaging the same segments of apical dendrites of GCs sparsely labeled with EGFP every other day during the 9 days of the difficult discrimination task or passive experience. Structural imaging was done before the odor experiment sessions. Addition and elimination of dendritic spines across days were measured by the scorers who were blind to the experimental condition.

We observed a notable increase in the density of apical dendritic spines in abGCs during learning (Fig. 3, A and B, and fig. S4F; $n = 33$ dendrites from eight mice). At the end of the 9-day learning, the spine density in abGCs increased on average by ~60%. In contrast, the abGC spine density was more stable in the passive experience group, showing only a mild increase (~15%) that was significantly lower than in the learning group (Fig. 3B and fig. S4A; $n = 20$ dendrites from four mice). Furthermore, we also observed an increase of ~40% in the spine density in basal dendrites of abGCs over 9 days of learning but not in the passive group (Fig. 3C and fig. S4, D, E, and G). Apical dendritic spines are the primary site of GC-mediated lateral inhibition of mitral/tufted cells, and thus, in this study, we focused the subsequent analysis on apical dendritic spines.

The increase of spine density in apical dendrites during learning was mediated partially by an increase in the formation of new spines and partially by a decrease in the spine elimination (Fig. 3, D to F, and fig. S4H), suggesting that learning promotes both formation and stabilization of abGC spines.

In a separate cohort of mice, we monitored the structural dynamics of apical dendrites of rGCs. During both learning and passive experience, rGCs showed a limited increase in the spine density, similar to the abGC passive group and significantly less than the abGC learning group (Fig. 3B and fig. S4, B and C. Task: $n = 26$ dendrites from six mice. Passive: $n = 18$ dendrites from three mice). Together, these results indicate that abGCs, but not rGCs, selectively exhibit context-dependent structural plasticity, with a substantially enhanced level of spine density increase during learning.

Next, we examined the relationship between the structural plasticity of abGC dendrites and the behavioral performance. We found a strong and significant correlation between the behavioral performance (the average correct rate of the last 3 days of training) and the rate of spine density increase averaged across dendrites in each animal (Fig. 3G; $n = 8$ mice). This correlation between the spine increase and behavioral performance could originate from two distinct sce-narios. In one scenario, rewards drive the spine increase, and thus, a higher performance level results in a larger spine increase. In another scenario, the spine increase drives behavioral improvement. To disambiguate these possibilities, we first examined the relationship between the spine increase (from session N-2 to session N) and behavioral performance in previous sessions (sessions N-1 and N-2). We found no correlation between these two measures, failing to support the first scenario (Fig. 3H, left). In contrast, we found a significant correlation between the spine increase and improvement in behavioral performance (Fig. 3H, right). These results support the idea that the increase in spine density drives the improved ability for the mice to discriminate the odors.

We noticed that the degree of spine increase in abGCs during learning was heterogeneous across abGCs imaged in each mouse and also across mice. In particular, we found that a large fraction of apical dendrites showed only mild increases, with another smaller fraction of dendrites showing marked increases (Fig. 4A). This led us to hypothesize that spine increases may occur preferentially in abGCs that respond to the odorants applied during learning. To address this hypothesis, we labeled a sparse set of abGCs with GCaMP6s ($n = 30$ dendrites in three mice). We were able to use GCaMP6s fluorescence to record the activity of abGC dendrites and also to perform a structural analysis of the imaged dendrites and their spines (Fig. 4B and see Materials and Methods). Similar to the somatic imaging experiments (Fig. 2B), we found that a subset of imaged dendrites responded to the applied odors in either an excitatory or a suppressive manner. We found that odor-excitatory dendrites demonstrated a significantly higher increase in the spine density than odor-suppressive and nonresponsive dendrites (Fig. 4C).

Collectively, these results demonstrate that abGCs, but not rGCs, show context-dependent plasticity of dendritic spines during learning but not during passive experience. The spine density increase was particularly prominent in the abGC dendrites that showed excitatory responses to the learned odors and in animals that learned to become more proficient in discriminating the odors.

Task engagement elevates the activity of piriform feedback

Having demonstrated that abGCs exhibit context-dependent plasticity, we sought to identify the mechanism by which behavioral context affects the level of abGC plasticity. GCs receive various types of feedback from the central brain, and one of the most abundant of these feedback projections is the glutamatergic feedback from the piriform cortex that synapses on the basal dendrites of GCs (2). We hypothesized that the context dependence of abGC plasticity could result from context-dependent activity of piriform feedback. Thus, we began by investigating the activity of piriform feedback to the GC layer.

We labeled piriform cortical neurons with GCaMP7b by injecting AAV-*hSyn*-GCaMP7b into the piriform cortex. Five weeks after the AAV injection, we were able to identify axonal boutons expressing GCaMP7b in the GC layer of the olfactory bulb and image their activity in vivo (Fig. 5A). Using this approach, we compared the activity of piriform feedback in task mice ($n = 456$ boutons in six mice) and in passive experience ($n = 678$ boutons in five mice) (Fig. 5B). We focused our analysis on the boutons that we were able to repeatedly identify longitudinally (see Materials and Methods). Piriform feedback boutons showed excitatory and suppressive responses to odors in both passive and task conditions (Fig. 5C). We found that the fraction of responsive odor-bouton pairs on each day
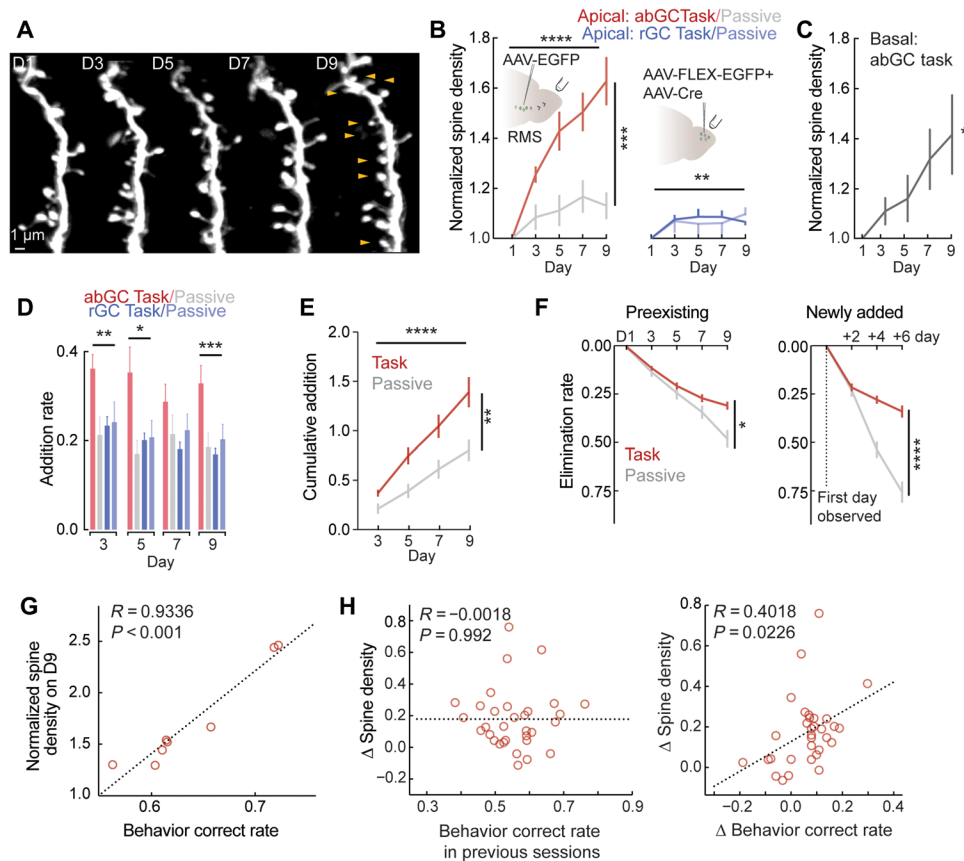
Fig. 3. abGCs increase spine density during learning. (**A**) Example in vivo images of one abGC dendrite over 9 days of task. Arrowheads point to some of the new spines that formed during the 9 days. (**B**) Normalized spine density of abGC apical dendrites and rGC apical dendrites during task and passive experience. Red, abGC task ($n = 33$ dendrites from eight mice); gray, abGC passive ($n = 20$ dendrites from 4 mice); dark blue, rGC task ($n = 26$ dendrites from six mice); light blue, rGC passive ($n = 18$ dendrites from three mice); two-way ANOVA in abGCs, $p_{(group)} < 0.001$ and $p_{(time)} < 0.0001$; rGCs, $p_{(group)} > 0.05$ and $p_{(time)} < 0.01$; abGC task and rGC task, $p_{(group)} < 0.0001$ and $p_{(time)} < 0.0001$. Mean ± SEM. (**C**) Normalized spine density of abGC basal dendrites during task. One-way ANOVA, $P = 0.0379$ ($n = 7$ dendrites from three mice). Mean ± SEM. (**D**) Fraction of added spines between each pair of adjacent imaging sessions normalized to the spine density on D1 of abGC and rGC dendrites during task and passive experience. Red, abGC task; gray, abGC passive; dark blue, rGC task; light blue, rGC passive. One-way ANOVA for each time point: D3, $P < 0.01$; D5, $P = 0.0104$; D7, $P > 0.05$; D9, $P < 0.001$. Learning increases spine addition rate in abGCs. Mean ± SEM. (**E**) Cumulative addition rate of abGC dendritic spines in the task (red) and passive (gray) condition. Two-way ANOVA, $p_{(group)} < 0.01$ and $p_{(time)} < 0.0001$. Mean ± SEM. (**F**) Fraction of eliminated spines between each pair of adjacent imaging sessions in abGCs for preexisting spines (spines that existed on D1, left) and newly added spines (right) in task (red) and passive (gray) conditions. Newly added spines that appeared on D3, D5, and D7 were pooled and aligned to the first imaging session in which each spine was observed. Preexisting spines: two-way ANOVA, $p_{(group)} = 0.0152$; newly added spines: mixed-effects analysis (see Materials and Methods), $p_{(group)} < 0.0001$. Learning stabilizes abGC spines. Mean ± SEM. (**G**) Behavioral performance (average correct rate of the last 3 days of learning) and the normalized spine density at D9 of abGCs show a significant positive correlation. Each data point represents one mouse ($n = 8$ mice). (**H**) Spine density increase between each pair of adjacent imaging sessions does not correlate with the behavioral performance in the previous session (left) but shows a significant positive correlation with behavioral performance increase across the two sessions. Each data point represents one pair of adjacent imaging sessions per mouse ($n = 32$ session pairs from eight mice). *, $P < 0.05$, **, $P < 0.01$, ***, $P < 0.001$, ****, $P < 0.0001$.

was significantly higher in the task condition than in passive experience. This difference was primarily driven by a larger number of excitatory responsive odor-bouton pairs in the task condition compared to passive experience. The suppressive responsive fraction was also higher in the task condition, although this difference was not statistically significant (Fig. 5D). In addition to the larger fractions of responsive odor-bouton pairs, responsive odor-bouton pairs showed stronger responses in the task condition, especially in the excitatory responsive odor-bouton pairs (Fig. 5, E to H). These results indicate that the activity of piriform feedback to GCs, especially the excitatory activity, is elevated during learning compared to passive experience. Thus, piriform feedback could potentially provide the context information to drive the observed context-dependent plasticity of abGC dendrites.

Collectively, we found that the activity of piriform feedback, especially excitatory activity, is enhanced during task compared with passive experience. Considering that the abGC dendrites with excitatory odor-evoked activity show particularly strong spine increases during learning (Fig. 4), we hypothesized that piriform feedback might be an essential source of context information, instructing the context specificity of abGC plasticity.

Task-dependent abGC plasticity requires piriform feedback activity

A prediction of our hypothesis is that disruption of piriform feedback during learning would interfere with normal learning-related plasticity of abGCs. To test this idea, we performed optogenetic inactivation of axon terminals of piriform feedback in the olfactory
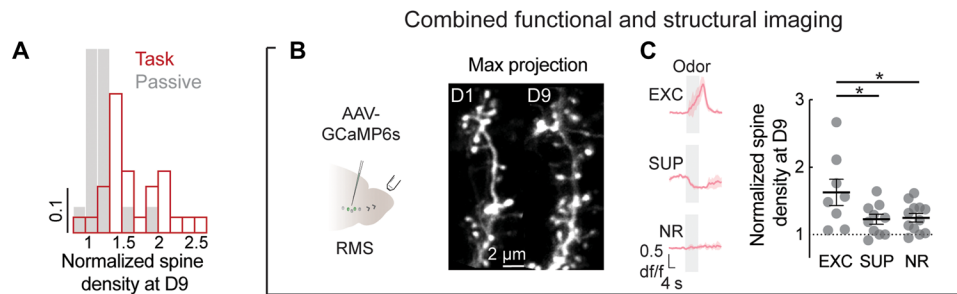
Fig. 4. Spine density increase during learning occurs preferentially in abGCs with excitatory odor responses. (**A**) Histogram of the spine density on D9 (normalized to D1) of abGC dendrites at task (red, *n* = 33 dendrites) and passive (gray, *n* = 20 dendrites) experience. Spine increase rate during task learning is heterogeneous. (**B**) Left: Schematic of the viral injection to label abGCs with GCaMP6s. Right: Example in vivo images of one GCaMP6s-labeled, odor-excited abGC dendrite on D1 and D9 of task. (**C**) Left: Example traces of dendrites showing excitatory odor activity (EXC), suppressive (SUP) odor activity, and not responsive (NR). Mean ± SEM. Right: Spine density at D9 (normalized to D1) of abGC dendrites that showed excitatory (*n* = 8 dendrites) or suppressive (*n* = 10 dendrites) odor activity or not responsive (*n* = 12 dendrites) to odors. One-way ANOVA, *P* = 0.0304. Holm-Šídák's multiple comparison test, $p_{(odor vs. ITI)}$ = 0.0316, $p_{(odor vs. NR)}$ = 0.0316. Spine increase is stronger in abGCs with excitatory odor responses. Mean ± SEM. *, *P* < 0.05.

bulb during learning. We only inactivated and imaged the right olfactory bulb unilaterally in an attempt to minimize the effect of inactivation on behavioral performance. To express the inhibitory opsin halorhodopsin (eNpHR) selectively in glutamatergic neurons in the piriform cortex, we used a transgenic line, Vglut2-Cre (*33*) and injected AAV encoding halorhodopsin in a Cre-dependent manner (Fig. 6, A and B). In another set of experiments, we injected AAV encoding nonconditional halorhodopsin in wild-type mice. The results were similar from these two sets of experiments, and thus, they were pooled. A separate injection of AAV-CB7-EGFP in the RMS was made to label abGCs.

After the pretraining period, we optogenetically inhibited the terminals of piriform feedback axons unilaterally in the right olfactory bulb using a 590-nm light-emitting diode (LED) light during the difficult discrimination task (Fig. 6C). The light was applied during the odor period of each trial in each session over 9 days. In a separate set of control animals, we expressed tdTomato instead of halorhodopsin in the piriform cortex (the control group). We imaged the dendritic spines of abGCs before the behavioral sessions every other day. This experiment was performed such that the experimenters were blind to the condition (experimental versus control).

Mice with disruption of the piriform feedback showed mild learning (D5 to D9 average correct rate, compared with chance level; *P* = 0.02, one-sample Wilcoxon signed-rank test), but these animals never achieved the control level of behavioral performance (Fig. 6D). The impairment of learning in the disruption animals did not reach statistical significance compared to controls, presumably because the undisrupted hemisphere was able to support learning. We found that disruption of piriform feedback significantly suppressed the apical spine density increase of abGCs (*n* = 36 dendrites in eight mice) compared to the control group (*n* = 37 dendrites in seven mice) (Fig. 6, E and F, and fig. S5A). The spine density in the feedback inhibition experiments was not significantly different from the mice that experienced the odors passively [Fig. 3B; two-way analysis of variance (ANOVA), $p_{(group)}$ = 0.355], suggesting that the decrease in plasticity is due to disruption of the feedback instead of changes in behavioral performance. We note, however, one potential caveat in this comparison is that mice in the passive group did not receive virus injection for piriform feedback labeling and LED during training. Together, these data show that the normal activity of piriform feedback is necessary for the context-dependent structural plasticity of abGCs.

Optogenetic activation of piriform feedback triggers learning-like plasticity in abGC dendrites

Next, we sought to test whether activation of piriform feedback during passive experience could artificially trigger learning-like plasticity in abGCs. To test this idea, we expressed the excitatory opsin ChrimsonR in glutamatergic neurons in the piriform cortex by injecting AAV-FLEX-hSyn-ChrimsonR-tdTomato in the piriform of Vglut2-Cre mice (Fig. 7, A and B). A separate injection of AAV-CB7-EGFP in the RMS was made to label abGCs. We activated piriform feedback by applying 660-nm LED light in the right olfactory bulb during the odor period in each trial for 9 days ("opto-pairing"), while the mice passively experienced the difficult discrimination odors. In separate sets of animals, we performed two control experiments. In one control, we applied light during the intertrial intervals (ITIs) instead of the odor period in mice expressing ChrimsonR in the piriform cortex ("opto-ITI control"). In the second control, we applied light during the odor period in mice expressing tdTomato instead of ChrimsonR in the piriform cortex ("no-opsin control") (Fig. 7C). We imaged the dendritic spines of abGCs before the experimental sessions every other day.

We found that activation of piriform feedback paired with odor stimulus significantly increased the apical spine density of abGCs (*n* = 41 dendrites in eight mice) compared with the opto-ITI control (*n*= 25 dendrites in four mice) and no-opsin control (*n* = 12 dendrites in three mice) (Fig. 7, D to F, and fig. S5B). The spine density increases in the controls were equivalent to the passive experience animals [Fig. 3B; two-way ANOVA, $p_{(group)}$ = 0.873]. Thus, activation of piriform feedback during the odor period was sufficient to trigger learning-like plasticity in abGC dendrites. However, we note that the increase in the spine density in the opto-pairing group (~30%) was less than what was observed in learning animals with good behavioral performance (Fig. 2H). This could be due to the artificial nature of our feedback activation where all axons expressing the opsin are synchronously activated and/or additional actions of other feedback mechanisms (e.g., glutamatergic feedback from other areas and neuromodulatory feedback) that are not assessed in this study.

Next, we examined whether the artificial pairing of piriform feedback activation with passive odor experience, which triggered learning-like structural plasticity, was sufficient to trigger functional plasticity of abGCs. To test this possibility, we expressed GCaMP6f
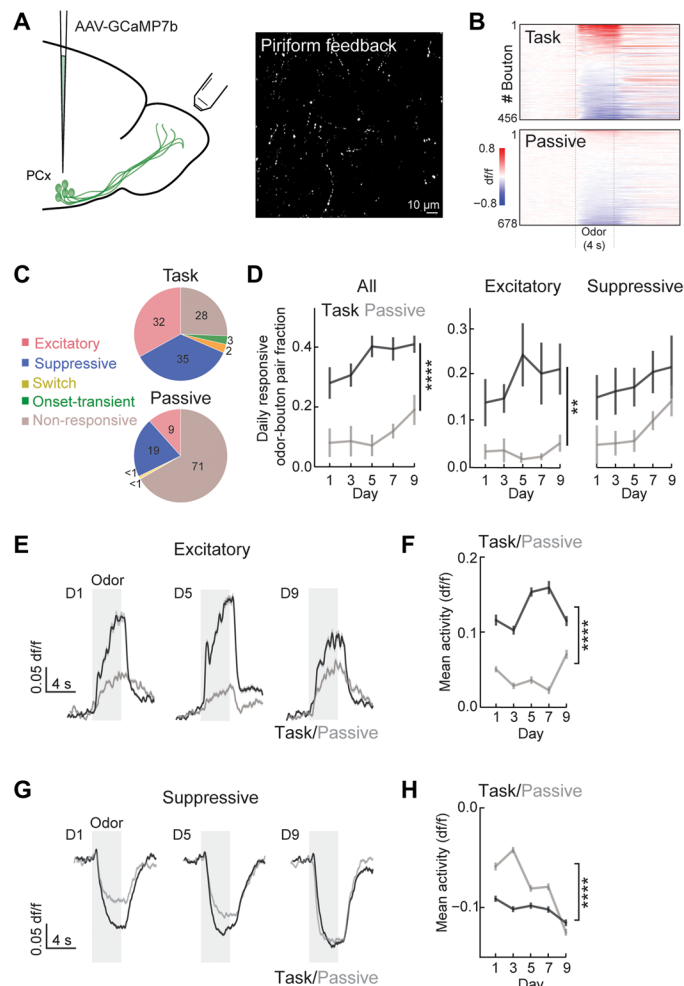
Fig. 5. Task engagement elevates the activity of piriform feedback. (A) Left: Schematic of the viral injection to label piriform feedback with GCaMP7b [piriform cortex (PCx)]. Right: Example in vivo image of piriform feedback axonal boutons expressing GCaMP7b in the GC layer of the olfactory bulb. **(B)** Activity heatmap of all boutons in task and passive experience on D5 to one odor (heptanal, 54%/ethyl tiglate, 46%). Each row corresponds to the trial-averaged activity of a single bouton. **(C)** Pie charts showing fractions of odor-bouton pairs that showed excitatory (red), suppressive (blue), switch (yellow), and onset-transient (green) responses, and not-responsive (light brown) in task and passive conditions. Numbers in the pie charts are the percentages of different categories. In total, there are 7808 odor-bouton pairs in the task condition and 5424 odor-bouton pairs in the passive condition. **(D)** Fraction of responsive odor-bouton pairs in task (black, $n = 6$ mice) and passive (gray, $n = 5$ mice) conditions. Mixed-effects analysis (see Materials and Methods); all activity, $p_{(group)} < 0.0001$; excitatory, $p_{(group)} < 0.01$; suppressive, $p_{(group)} = 0.1057$. Task engagement enhances excitatory activity of piriform feedback. Mean ± SEM. **(E)** Average population activity of excitatory odor-bouton pairs during task (black) and passive (gray) at D1, D5, and D9. Gray box, the odor period. Mean ± SEM. **(F)** Mean activity (df/f) during the odor period of excitatory odor-bouton pairs during task (black, $n = 890$ pairs) and passive (gray, $n = 496$ pairs). Two-way ANOVA, $p_{(group)} < 0.0001$. Mean ± SEM. **(G)** Average population activity of suppressive odor-bouton pairs during task (black) and passive (gray) at D1, D5, and D9. Gray box, the odor period. Mean ± SEM. **(H)** Mean activity (df/f) during the odor period of suppressive odor-bouton pairs during task (black, $n = 1234$ pairs) and passive (gray, $n = 951$ pairs). Two-way ANOVA, $p_{(group)} < 0.0001$. Mean ± SEM. **, $P < 0.01$, ****, $P < 0.0001$.

in abGCs and repeated the opto-pairing protocol to activate piriform feedback during the odor period during passive experience for 9 days in animals expressing ChrimsonR in piriform feedback. On D10, we imaged GCaMP6f responses during passive experience without the optogenetic stimulation to examine the potential effect of the prior pairing of odor and feedback activation on abGC responses (Fig. 7G). We found that a significantly higher fraction of odor-abGC pairs showed excitatory responses in the opto-pairing group ($n = 5$ imaging fields in three mice) than in the passive group (Fig. 7, H and J; $n = 6$ imaging fields in six mice). Furthermore, these excitatory responsive abGCs showed stronger odor responses in the odor-pairing group than in the passive group (Fig. 7I). We note that it is possible that stimulation of feedback fibers in the bulb elicited plasticity within the piriform cortex, which could have contributed to the augmented odor responses of abGCs. Together, optogenetic pairing of piriform feedback with passive odor experience was sufficient to trigger learning-like structural and functional plasticity of abGCs.

Piriform feedback elicits stronger excitatory postsynaptic currents in abGCs than rGCs in acute slices from naive animals

Our results indicate that the elevated activity of piriform feedback during learning promotes the plasticity of abGCs but not rGCs. How does piriform feedback selectively enhance abGC plasticity? As a potential mechanism for this cell-type specificity (abGCs versus rGCs), we considered the possibility that piriform feedback preferentially excites abGCs. A previous study has shown that learning strengthens feedback inputs on abGCs from piriform and anterior olfactory cortex (18); however, here, we reasoned that such a difference should also exist before learning of the task.

As detailed in Supplementary text, we prepared acute olfactory bulb slices from naive animals and performed whole-cell patch-clamp electrophysiological recordings from abGCs and rGCs (fig. S6) as we optogenetically activated piriform feedback axons. We found that the magnitude of optically evoked current was greater in abGCs compared with rGCs, and the latency to current onset was smaller. Although these results do not specify the origin of the observed differences, they nonetheless indicate that in naive mice, abGCs are more strongly excited by piriform feedback than rGCs. This cell-type specificity could be a basis for the stronger sensitivity of abGC plasticity to behavioral context.

DISCUSSION
Here, we investigated the in vivo dynamics and mechanisms of plasticity of abGCs in the olfactory bulb. Toward this goal, we combined learning of difficult olfactory discrimination, longitudinal structural, and functional imaging of individual abGCs, as well as imaging and manipulation of feedback from the piriform cortex. This approach revealed that discrimination learning increases the responses of abGCs and decreases the responses of rGCs to the learned odors. This increase in abGC responses was accompanied by an increase in the apical dendritic spine density of abGCs that synapse with lateral dendrites of mitral cells. This spine increase was especially strong in the abGCs that show excitatory responses to the learned odors. Such a spine increase was not observed in abGCs when mice experienced the same odors passively nor was it found in rGCs. We further demonstrated that the context specificity of abGC
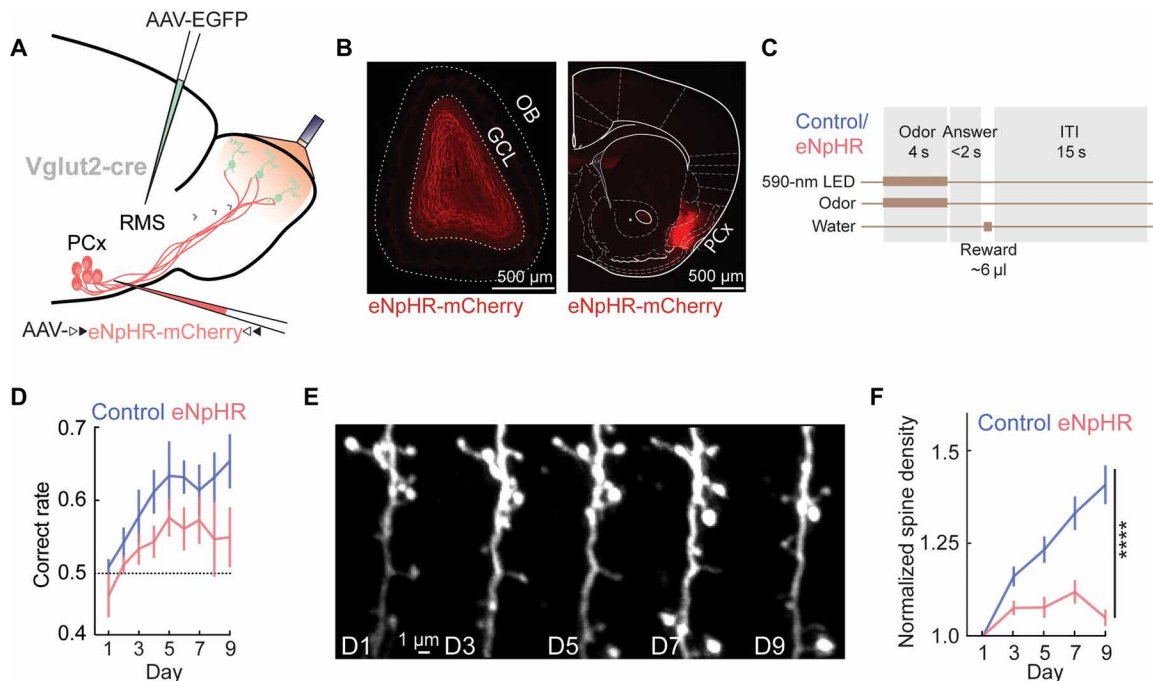
Fig. 6. Optogenetic inactivation of piriform feedback abolishes task-dependent abGC plasticity. (**A**) Schematic of the optogenetic inactivation experiment. AAV-EGFP was injected to the RMS to label abGCs and AAV-FLEX-halorhodopsin-mCherry (eNpHR) was injected to the PCx to express eNpHR in piriform feedback. (**B**) Images of histological sections showing the expression of halorhodopsin-mCherry (eNpHR) in the PCx neurons (right) and their axonal terminals in the GC layer (GCL) of the olfactory bulb (OB) (left). (**C**) Trial structure of optogenetic inactivation experiments. (**D**) Behavioral performance of mice in the eNpHR-expressing group (red, $n = 8$ mice) and control group (blue, $n = 7$ mice). Dotted line represents the chance level. Mixed-effects analysis (see Materials and Methods), $p_{(group)} = 0.1483$. There is a nonsignificant trend that unilateral inactivation of piriform feedback impairs learning. Mean ± SEM. (**E**) Example in vivo images of one abGC dendrite of feedback inactivation experiments during learning. (**F**) The spine density (normalized to D1) of abGC dendrites in mice in the eNpHR-expressing group (red, $n = 36$ dendrites in eight mice) and the control group (blue, $n = 37$ dendrites in seven mice). Two-way ANOVA, $p_{(group)} < 0.0001$. Mean ± SEM. ****, $P < 0.0001$.

spine plasticity is instructed by feedback from the piriform cortex to the olfactory bulb that preferentially excites abGCs over rGCs, and inactivation of piriform feedback during learning prevented normal abGC plasticity, while activation during passive experience induced learning-like abGC plasticity.

Context specific plasticity of abGCs

Previous studies with slice electrophysiology and postmortem histology showed that young abGCs are highly plastic (*11*, *32*) and that learning induces spine density increase in abGCs (*30*, *34*). Here, our in vivo longitudinal imaging showed that the spine increase in abGCs occurs gradually and cumulatively over days of perceptual learning by increasing new spine formation and decreasing spine elimination. Furthermore, we combined functional and structural imaging and found that learning induces cell-specific effects, where abGCs that show excitatory responses to the learned odors preferentially and markedly increase their spine density. A recent study suggested that the survival of abGCs is nonselective (*35*). However, our results indicate that learning does not increase the connectivity of surviving abGCs homogeneously. Rather, learning selectively incorporates those abGCs that respond to the learned odors into the bulbar circuit, presumably to generate an inhibitory circuit that is useful for the discrimination of these particular odors. Together with previous studies that demonstrated that learning can enhance the responses of abGCs to the learned odors (*23*, *34*, *36*, *37*) and increase the connectivity of abGCs with mitral cells (*38*), we pro-

pose that abGC plasticity during learning establishes an inhibitory circuit that selectively responds to the learned odors, which could provide selective inhibition to responsive mitral cells.

It is established that mitral cells enhance their pattern separation during perceptual learning to discriminate similar odorants (*4*–*6*). Mitral cell pattern separation likely involves lateral inhibition provided by GCs. We recently demonstrated that genetically ablating young adult-born neurons reduces pattern separation of mitral cells and impairs behavioral performance in difficult discrimination (*27*). The stronger and faster abGC responses acquired during learning likely contribute to the enhanced pattern separation of mitral cells and rapid behavioral discrimination. We propose that highly plastic abGCs are selectively integrated in a context-dependent manner to generate specific inhibitory circuits that facilitate mitral cell pattern separation. In contrast to other sensory systems in which each stimulus is continuous and has high degrees of correlations (e.g., the spatiotemporal correlation of visual stimuli), olfactory inputs are fundamentally combinatorial, where each stimulus activates a unique combination of discrete glomerular units. With ~1000 glomerular units, the possible number of these combinations is astronomically large, and it is also difficult to predict which of similar combinations need to be discriminated versus generalized at any given behavioral epoch. Because of continuous adult neurogenesis, the olfactory bulb always has young abGCs at the peak of their plasticity. Furthermore, the large number of young abGCs ensures that there are many patterns of initial connectivity of individual abGCs. Those
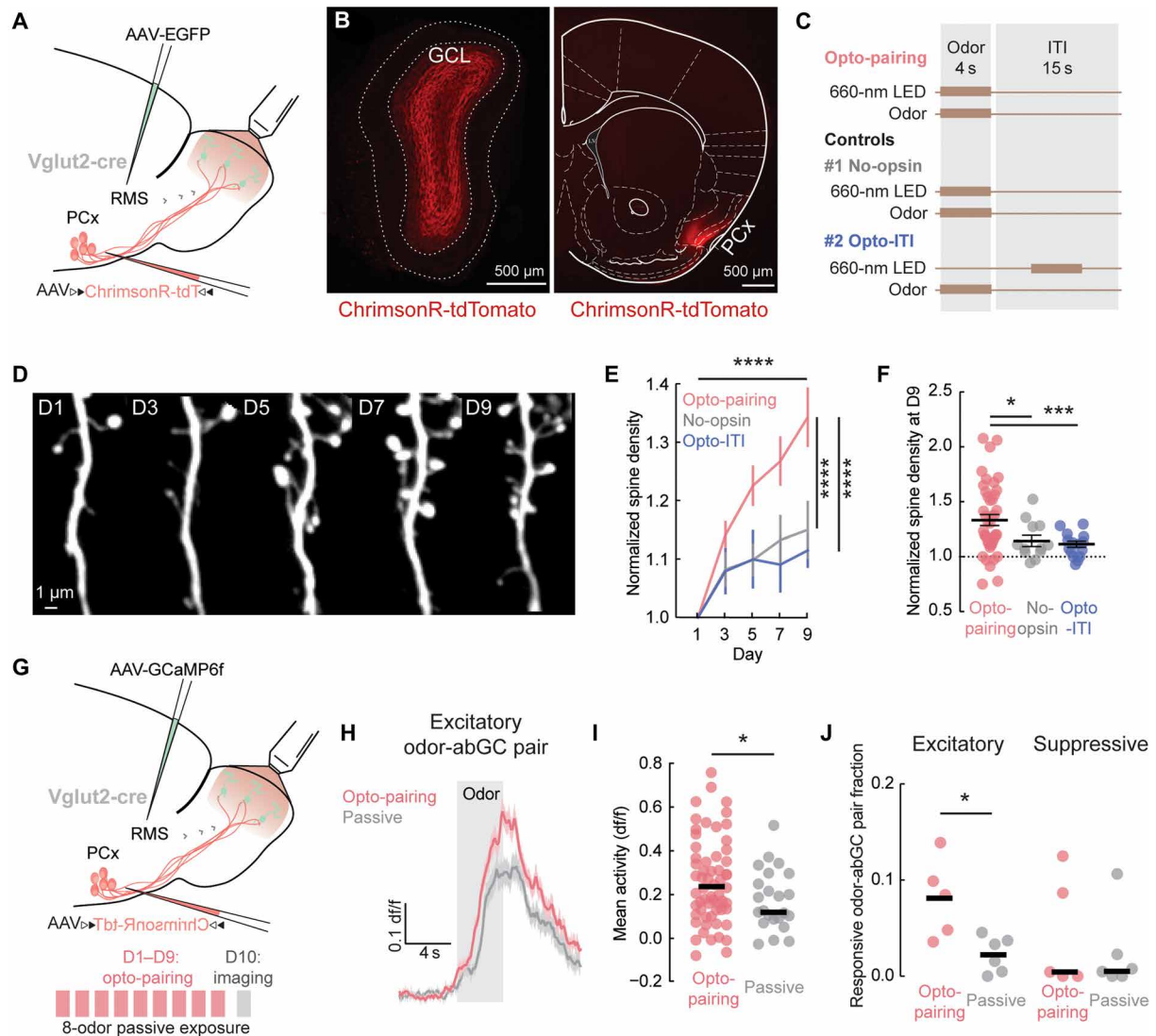
Fig. 7. Optogenetic activation of piriform feedback triggers learning-like plasticity in abGC dendrites. (**A**) Schematic of the optogenetic activation experiment. AAV-EGFP was injected to the RMS to label abGCs and AAV-FLEX-ChrimsonR-tdTomato was injected to the PCx to express ChrimsonR in piriform feedback. (**B**) Images of histological sections showing the expression of ChrimsonR-tdTomato in the PCx neurons (right) and their axonal terminals in the GCL of the olfactory bulb (left). (**C**) Schematic of the trial structure in the opto-pairing, the no-opsin control, and the opto-ITI control groups. (**D**) Example in vivo images of one abGC dendrite in the opto-pairing group during passive experience. (**E** and **F**) The spine density (normalized to D1) of abGC dendrites in mice in the opto-pairing group (red, $n = 41$ dendrites in eight mice) and two control groups (blue, opto-ITI group, $n = 25$ dendrites in 4 mice; gray, no-opsin group, $n = 12$ dendrites in three mice). (E) Two-way ANOVA, $p_{(group)} < 0.01$; $p_{(time)} < 0.0001$; multiple comparisons with Bonferroni-Šídák method, $p_{(opto-pairing\ vs.\ no-opsin)} < 0.0001$; $p_{(opto-pairing\ vs.\ opto-ITI)} < 0.0001$. Mean ± SEM. (F) one-way ANOVA, $P < 0.01$; multiple comparisons with Dunnett's method, $p_{(opto-pairing\ vs.\ no-opsin)} = 0.0299$; $p_{(opto-pairing\ vs.\ opto-ITI)} < 0.001$. Mean ± SEM. (**G**) Top: Schematic of the optogenetic activation and calcium imaging experiment. AAV-GCaMP6f was injected to the RMS to express GCaMP6f in abGCs and AAV-FLEX-ChrimsonR-tdTomato was injected to the PCx to express ChrimsonR in piriform feedback. Bottom: Timeline of the opto-pairing (D1 to D9) and imaging (D10). (**H**) Average population activity of excitatory odor-abGC pairs on D10, after 9 days of opto-pairing (red) or passive experience (gray). Mean ± SEM. (**I**) Mean activity (df/f) during the odor period of excitatory odor-abGC pairs after opto-pairing (red, $n = 60$ pairs) or passive experience (gray, $n = 21$ pairs). Welch's t test, $P = 0.0365$. Black lines represent the medians. (**J**) Fractions of responsive odor-abGC pairs after opto-pairing (red, $n = 5$ fields in three mice) or passive experience (gray, $n = 6$ fields in six mice). Mann-Whitney test: excitatory, $P = 0.0173$; suppressive, $P > 0.05$. Black lines represent the medians. *, $P < 0.05$, ***, $P < 0.001$, ****, $P < 0.0001$.

abGCs with the initial connectivity that can be refined to contribute to capricious behavioral demands may preferentially increase their apical spines and get incorporated into the bulbar circuit, while those abGCs whose initial connectivity is not useful may not get incorporated. This mechanism allows the olfactory bulb to adapt to a dynamic environment where the repertoire of behaviorally relevant odorants may continuously change.

Piriform feedback instructs the context-specificity of abGC plasticity

The observation that abGC plasticity is enhanced during learning but not during passive experience suggested that abGC plasticity is modulated by top-down information about the behavioral context. However, the mechanism that ensures the context specificity of abGC plasticity was unknown. Here, we demonstrated that the glutamatergic

feedback from the piriform cortex, which arrives at the perisomatic area and/or basal dendrites of GCs, is enhanced during learning and is necessary for learning-induced abGC plasticity and sufficient to induce learning-like abGC plasticity during passive experience. We note, however, that our results do not exclude additional contributions by other types of feedback pathways, such as glutamatergic feedback from the anterior olfactory nucleus and neuromodulatory feedback (*39*). We also found that the spine increase in the apical dendrites during learning is particularly enhanced in abGCs that show excitatory odor responses. Furthermore, artificial activation of piriform feedback was effective in inducing learning-like plasticity only when it was coincident with odor stimuli (opto-pairing) and not when they were temporally dissociated (opto-ITI control). These results indicate that piriform feedback alone is not sufficient to induce abGC plasticity. Rather, coincident excitatory inputs at both basal and apical dendrites, from piriform feedback and mitral cell feedforward inputs, respectively, drive the increase of apical dendritic spines. Such a cellular mechanism of coincidence detection can explain the two levels of specificity of abGC plasticity: Piriform feedback ensures that the plasticity is enhanced during learning, and feedforward inputs allow selective plasticity in abGCs that respond to the learned odor (Fig. 8).

Learning-induced plasticity is largely restricted to young abGCs compared to the general population of GCs (rGCs). How does task engagement enhance the plasticity of abGCs but not rGCs? In addition to the difference in their age, we note that abGCs and rGCs may include distinct, molecularly defined subsets of GCs (*40*). Regardless, our slice electrophysiological recordings provided a potential explanation for their differential sensitivity to context (figs. S6 and S7). Specifically, we found that abGCs are more strongly excited by the activation of piriform feedback than rGCs in acute olfactory bulb slices prepared from naive, untrained animals. Thus, it appears that abGCs have a privileged access to context-dependent modulation by piriform feedback. Future studies should identify the origin of this cell-type difference. Potential origins include a differential number or strength of synapses and intrinsic properties of abGCs versus rGCs. It also remains possible that piriform feedback has an additional level of selectivity. For example, it is possible that each piriform feedback axon selectively excites abGCs whose odor tuning matches that of the piriform axon (*41*). Such a selective wiring scheme would achieve an efficient way to enhance the plasticity of ta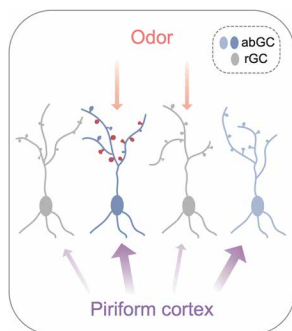sk-relevant abGCs. We also note that these results do not exclude additional mechanisms that differentially regulate the plasticity of abGCs and rGCs, such as intrinsic differences in gene expression patterns.

The idea that coincident excitatory inputs at basal and apical dendrites drive synaptic potentiation is reminiscent of previous work in pyramidal neurons. In these studies, it was shown that coincident inputs onto distal and proximal dendrites can interact superlinearly and drive dendritic plateau potentials, which induce large calcium influx and drive synaptic plasticity (*42*). For example, in the hippocampus CA1 region, coincidence of distal inputs from the entorhinal cortex and proximal inputs from the CA3 region onto CA1 pyramidal neurons drives dendritic plateau potentials and long-term potentiation, which underlies the generation of spatial selectivity of CA1 place cells (*43–45*). It appears that the olfactory bulb uses a similar cellular mechanism for coincidence detection of distal mitral cell inputs and proximal piriform inputs onto abGCs to drive robust synaptic plasticity in the abGCs appropriate for the behavioral context. A previous study proposed that proximal feedback inputs can relieve GC distal synapses from Mg^{2+} blockage of *N*-methyl-D-aspartate receptors (NMDA), providing a mechanism for superlinear interactions of GC proximal and distal inputs (*46, 47*).

Comparison with abGCs in the hippocampus

Aside from the olfactory bulb, the dentate gyrus of the hippocampus is the other mammalian brain area where substantial adult neurogenesis takes place, where new neurons differentiate into excitatory GCs, as opposed to inhibitory GCs in the olfactory bulb, throughout adulthood (*48*). Similarly to the olfactory bulb, dentate gyrus abGCs during their critical period exhibit a higher level of plasticity (*49, 50*). Behavioral experience affects the survival and integration of abGCs in the dentate gyrus (*51, 52*). For example, exercise and environmental enrichment can increase their connectivity to the cortex and other hippocampal areas, respectively (*52*). Ablating dentate gyrus abGCs impairs fine, but not easy, spatial pattern discrimination (*53*) and augmenting adult neurogenesis can improve discrimination of similar environments (*52, 54*). These findings suggest that adult neurogenesis in both olfactory bulb and dentate gyrus provides animals with a higher degree of flexibility to cope with the complex and dynamic environment. It will be interesting to test whether the plasticity mechanisms revealed in this study of the olfactory bulb abGCs are shared with dentate gyrus abGCs.

Although adult neurogenesis is restricted to few areas in the mammalian brain, all brain areas maintain certain degrees of plasticity throughout life. The mechanisms studied here represent a marked example of a common strategy by which the brain refines its circuitry to adapt to continuous and capricious changes in the environment.

Fig. 8. Model schematic. Schematic of the proposed mechanisms for the context-dependent, cell-type specific plasticity. Coincidence of odor input and context-dependent piriform feedback input leads to increased apical spine density (red) and stronger and faster responses (shown by darker color) of abGCs.

MATERIALS AND METHODS
Materials availability statement
Animals
All procedures were in accordance with protocols approved by the Institutional Animal Care and Use Committee at University of California San Diego. Mice were acquired from Charles River (C57BL/6 wild-type) and the Jackson laboratory (Vglut2-ires-cre knock-in). All surgeries and experiments were carried out in adult mice (around 8 weeks old). Mice were housed in plastic cages with standard bedding in a room with a reversed light cycle (12-12 hours).

All experiments were performed during the dark period. All mice were prepared exclusively for the experiments described in this paper. Littermates or sexes were not paired for particular experiments. Health conditions of mice were monitored daily during training. Both male and female mice were used.

Surgeries and viral injections

Craniotomy. Mice were anesthetized with isoflurane (3% induction, ~1% maintenance). A custom made stainless-steel headplate was secured onto the exposed skull with superglue. A craniotomy was made above the right olfactory bulb. A glass window was placed in the craniotomy, sealed with vetbond, and secured with dental cement. Baytril (10 mg/kg) and buprenorphine SR (0.5 mg/kg) were subcutaneously injected at the end of the surgery.

Injections. Glass pipette was made from thin-walled glass capillary tubing (Wiretrol II, PA) using a horizontal puller (P-2000, Sutter Instruments, CA, USA). Viral injections were made with a custom injector through a glass pipette (~20 µm in diameter) at a speed of 20 nl/1.5 min. After the injection (5 to 10 min), the pipette was retracted from the brain. For deep brain injections, including RMS and piriform cortex injections, mice were first stereotaxically injected with viruses before the headplate implantation. To target the piriform cortex, three injections were made at (from bregma: anterior-posterior/medial-lateral/dorsal-ventral) 2.8/1.5/3.0 mm, 2.2/2.0/3.5 mm, and 1.8/2.5/4 mm (*10*). For the RMS injections to label abGCs, the injector was placed at an 11° angle (from the perpendicular position) and injected from the posterior side toward the inferior cerebral vein (ICV). The injection sites were 0.54-mm posterior to ICV and 0.9 to 1 mm from the midline and 2.7-mm deep from the dura. We found that using the ICV as the reference to target the RMS was more reliable than using the bregma as the landmark, although no statistical comparisons were performed.

For the olfactory bulb injections to label rGCs, pipettes (tips were sharpened to 45° to 60° angle using a custom rotation disk) were used to penetrate the dura after the skull was peeled during the craniotomy. The injection site was targeted at the center of the GC layer at the center of the olfactory bulb at 0.4-mm underneath the dura.

Viruses. All viruses were acquired from Addgene unless stated otherwise. For functional imaging of abGCs, AAV1-CAG-GCaMP6f (catalog no. 100836), AAV1-hSyn-GCaMP6f (catalog no. 100837), or AAV1-hSyn-GCaMP6s (200 nl; catalog no. 100843) were used. For functional imaging of rGCs, 1:100 mixtures of AAV1-CMV-Cre (catalog no. 105537) and AAV1-hSyn-FLEX-GCaMP6f (20 nl per site; catalog no. 100833) were used. For structural imaging of abGCs, AAV2/1-CB7-EGFP (120 to 150 nl; catalog no. 105542) was used. For structural imaging of rGCs, 1:1000 mixtures of AAV1-CMV-Cre and AAV2/1-CAG-FLEX-EGFP (20 nl per site; catalog no. 51502) were used. For functional imaging of piriform feedback, AAV1-hSyn-GCaMP7b (100 nl per site; catalog no. 104489) was used. For optogenetic activation experiments, AAV5-hSyn-FLEX-ChrimsonR-tdTomato (150 nl per site; catalog no. 62723, for Vglut2-cre mice) was used. For optogenetic inactivation experiments, AAV2/1-hSyn-FLEX-halorhodopsin-mCherry (150 nl per site; catalog no. AAV85, for Vglut2-cre mice) or 1:1 mixture of AAV2/1-hSyn-FLEX-halorhodopsin-mCherry with AAV1-CMV-Cre (150 nl per site) (for B6 mice) were used. For optogenetic control experiments, AAV2/1-CAG-FLEX-tdTomato (150 nl per site; catalog no. 51503, for Vglut2-cre mice) was used.

Surgeries for slice electrophysiology experiments. For slice electrophysiological experiments to excite piriform feedback and record whole-cell patch-clamp from abGCs and rGCs, Vglut2-cre mice were injected with AAV-hSyn-FLEX-ChrimsonR-tdTomato (150 nl per site) bilaterally to label piriform feedback at 5 weeks before the recording date. At 3 weeks before the recording date, a second injection at the RMS with AAV-CB7-EGFP (150 to 200 nl) was performed to label abGCs. The skin on the skull was sutured after each injection.

BrdU analysis

BrdU treatment. To validate the effectiveness of abGC labeling, mice were treated with BrdU (Sigma-Aldrich, B5002) daily starting from 10 to 14 days before viral injection, and for 3 days after injection, and sacrificed 4 weeks later for immunostaining. Each mouse received BrdU (approximately 0.2 mg/g body weight/day) in the drinking water with the BrdU concentration of 1 mg/ml.

Immunohistochemistry. Coronal sections (45 µm thick) of the olfactory bulb were prepared with a microtome and later mounted on microscopic slides. For immunostaining, sections were incubated in primary antibodies overnight and then in secondary antibodies for 2 hours at room temperature. For BrdU staining, sections were incubated in HCl (2 N) at 37°C for 30 min and treated with 0.5 M borate buffer (pH 8.5) (boric acid, Sigma-Aldrich, B9645) for 10 min before incubation with primary antibodies. Primary and secondary antibodies were diluted in a blocking buffer [0.3% Triton X-100, 1% serum from the same species as secondary antibody, 0.1% bovine serum albumin, and 0.1 M phosphate-buffered saline (PBS) (pH 7.4)]. BrdU: primary (rat, Abcam), 1:200; secondary (donkey anti-rat, Alexa 594–conjugated, Invitrogen), 1:1000. GFP: primary (chicken, Aves), 1:400; secondary (donkey anti-chicken, Alexa 488, Jackson ImmunoResearch), 1:1000.

Imaging and cell counting. Ten sections for each animal were randomly chosen for imaging and quantification. Zeiss Apotome fluorescence microscope with a 20× objective was used to capture z-stack images with a step size of 1.5 µm. The quantification of GFP- and BrdU-positive cells was manually performed with ImageJ. The image acquisition and cell counting were performed by experimenters who were not informed of the purpose of this experiment.

Slice electrophysiology experiments

Olfactory bulb slicing. Mice were deeply anesthetized with euthasol (150 mg/kg, intraperitoneally) and transcardially perfused with 15 ml of ice-cold modified artificial cerebrospinal fluid (ACSF) [composition: 75 mM sucrose, 87 mM NaCl, 25 mM NaHCO₃, 2.5 mM KCl, 1.3 mM NaH₂PO₄·H₂O, 7 mM MgCl₂·6H₂O, 0.5 mM CaCl₂·2H₂O, and 5 mM ascorbic acid, in ddH₂O; osmolarity of 320 to 328 mOsm (pH 7.3 to 7.4)] saturated with carbogen gas (95% oxygen and 5% carbon dioxide). The brain was then rapidly dissected from the cranial cavity, and coronal slices with a thickness of 300 µm containing the olfactory bulb were prepared on a semiautomatic vibrating blade microtome (VT1200, Leica, IL, USA). Brain slices were maintained in ACSF [composition: 126 mM NaCl, 2.5 mM KCl, 26 mM NaHCO₃, 1.25 mM NaH₂PO₄·H₂O, 1 mM MgCl₂·6H₂O, 2.4 mM CaCl₂·2H₂O, and 10 mM glucose, in ddH₂O; osmolarity, 299 to 301 mOsm (pH 7.30 to 7.40)] saturated with carbogen gas in a water bath at 30° to 32°C for at least 1 hour before electrophysiological recording commenced. Once in the recording chamber, olfactory bulb slices were continually perfused with carbogen-saturated ACSF (containing 100-µm picrotoxin) via a peristaltic pump (Minipuls3; Gilson, WI, USA) at 31 ± 1°C.

Recording. A horizontal puller (P-97, Sutter Instruments, CA, USA) was used to shape thin-walled borosilicate glass capillary tubing into microelectrodes for recording, which had resistance values

of 5 to 7 megohm when filled with internal solution (composition: 125 mM potassium gluconate, 20 mM Hepes, 10 mM NaCl, 3 mM Mg-ATP, 2 mM Alexa Fluor 350, and 0.1% neurobiotin (pH 7.31; 284 mOsm). Whole-cell patch-clamp recordings were made from visually identified GFP$^+$ and GFP$^-$ neurons in the granule layer of the olfactory bulb. Neurons were visualized using an upright microscope (Scientifica, UK) equipped with infrared differential interference contrast optics and a Q-imaging Retiga Exi camera (Q Imaging, Canada). Neurons were identified as GFP$^+$ through a 40× water-immersion objective using fluorescence illumination from a 470-nm LED light source (pE-100; CoolLED, NY, USA). Signals were amplified using a Multiclamp 700B amplifier (Molecular Devices, CA, USA), low-pass–filtered at 3 kHz, digitized at 10 kHz using a Digidata 1550, and recorded using pClamp 10.4 software (Molecular Devices, CA, USA). Series resistance [GFP$^+$ abGCs: 26.26 megohm ±11.07 (SD); GFP$^-$ putative rGCs: 26.24 megohm ±11.37 (SD)], input resistance, and holding current were monitored throughout experiments via a 5-mV 100-ms step. Any recordings with series resistance >45 megohm were excluded from analysis. Any significant changes (>25%) in these measures were taken as signs of cell deterioration and recordings were terminated. Neurons were recorded in voltage-clamp mode at a holding potential of −70 mV, and current was injected in current-clamp mode to give a resting potential of ~−65 mV.

Optogenetic activation. ChrimsonR-expressing terminals were activated by a 589-nm diode-pumped solid-state laser (OEM Laser Systems, UT, USA) controlled using a Master-8 pulse stimulator (A.M.P.I., Jerusalem, Israel). Light was delivered via a 300-μm optic fiber resting on the slice. To assess the response to optical activation of ChrimsonR terminals, a light pulse train consisting of 25 pulses at 25 Hz (5-ms pulse duration, 10-mW light power at the fiber tip) was delivered to the slice every 30 s. In voltage-clamp and current-clamp mode, ~10 to 15 sweeps were collected, and an average response was calculated.

Post hoc histology. Following the recording, brain slices were fixed in 4% paraformaldehyde overnight and then washed in PBS (4× 10 min). Slices were blocked in PBS containing 0.3% Triton X-100 (0.3% PBS-T) with 3% normal donkey serum (NDS; Jackson ImmunoResearch, USA) for 60 min at room temperature followed by incubation in 0.3% PBS-T with 3% NDS, CF633-conjugated streptavidin (1:1000; Biotium, CA, USA), and a DNA-specific fluorescent probe (4′,6-diamidino-2-phenylindole; 1:50,000) for 90 min at room temperature. Last, slices were washed in PBS (4× 10 min), then mounted onto glass microscope slides, and coverslipped using polyvinyl alcohol mounting medium with triethylenediamine (Sigma-Aldrich, MO, USA). A confocal laser scanning microscope (Zeiss 880) with ZEN software (Zeiss, Jena, Germany) was used to capture images of the olfactory bulb. High-magnification images of neurobiotin-filled neurons were obtained through a 40× water immersion objective using serial z-stack images with an optical slice thickness of 1.5 μm.

Odorant delivery
Odorants used in all pretraining, task, and passive experience were diluted in mineral oil (Thermo Fisher Scientific, O121-1) to achieve a vapor pressure of 200 parts per million (ppm). Using a custom-built olfactometer, saturated odorant vapor was mixed with filtered, humidified air at a 1:1 ratio to a final concentration of 100 ppm. A mass flow controller (Aalborg, New York) was used to control the airflow at 1 L/min.

Behavior
Behavioral tasks were identical to our previous study (*27*), except for the choice of the pretraining odors (below). Water restriction

started 3 to 5 days (for abGC-labeled mice) or 5 to 12 days (for rGC-labeled mice) after surgery and ~18 days before the beginning of behavioral training. Mice were given ~1 ml of water daily to maintain the bodyweight ≥75% of the initial value. A real-time system (C. Brody) was used to control the behavioral program. Two custom-made lick ports were installed with infrared beams to detect left and right licks. A correct trial (defined by the first lick during the answer period) was rewarded with ~6 μl of water. An incorrect trial was terminated upon an incorrect first lick during the answer period, and no reward or punishment was given. Mice were allowed to lick during the odor period, although only the first lick during the answer period was scored as their choice. Each mouse performed one session per day, which consisted of 150 trials unless the mouse disengaged earlier.

Pretraining: Licking. In the first behavioral session, mice were rewarded for licking either left or right lick ports during the 2-s answer period in each trial without any odorant stimuli. The ITI was gradually increased from 1 to 3 s. In the second session, cumene (Sigma-Aldrich, C87657) odorant was delivered for 4 s in each trial, and mice were rewarded for licking left during the 2-s answer period. A right lick during the answer period terminated the trial without punishment. The ITI was increased from 3 to 15 s in increments of 2 s and fixed at 15 s for the following sessions. In the third session, 2-hexanone (Sigma-Aldrich, AC146881000) odorant was delivered in each trial, and mice were rewarded for licking right.

Pretraining: Easy discrimination. Once mice performed above 90% correct in the licking sessions, they were trained to perform easy discrimination task in which either cumene or 2-hexanone was delivered in each trial. The odorant in each trial was chosen randomly with no more than three consecutive trials of the same odorant. Same as pretraining sessions, cumene corresponded to left-lick trials and 2-hexanone corresponded to right-lick trials. Mice were only rewarded for correct licks, and incorrect licks led to the termination of trial without punishment. Once mice reached >80% correct rate with the first set of easily discriminable odorants (3.17 ± 1.34 sessions, mean ± SD), an easy discrimination task was repeated with another set of odorants. Cyclohexanone (Sigma-Aldrich, 398241) signaled left-lick trials and isoamyl acetate (Sigma-Aldrich, C39601) signaled right-lick trials. Mice were trained on these new easily discriminable odorants until they reached >80% correct rate (2.12 ± 0.60 sessions).

Difficult discrimination. In each trial, one odorant from a panel of eight binary mixtures [heptanal (Sigma-Aldrich, H2120) (%)/ethyl tiglate (Sigma-Aldrich, W246000) (%): H54E46, H52E48, H51.5E548.5, H51E49, H49E51, H48.5E51.5, H48E52, and H46E54] was delivered in a predetermined, pseudo-random order with no more than three consecutive trials of odorants with the same lick side. Odorants with higher heptanal ratio signaled left-lick trials, and the odorants with higher ethyl tiglate ratio signaled right-lick trials. The rest of the settings were the same as the easy discrimination task. Mice were trained with this difficult discrimination task for nine sessions.

Passive experience. A separate cohort of mice went through the passive experience without task engagement but otherwise treated identically to task animals including water restriction. These mice were exposed to the same odorants within the same trial structure and session duration (150 trials) and under the same behavioral timeline (pretraining, easy discrimination to difficult discrimination) without engaging in the discrimination task. The median of easy discrimination task session numbers in task engagement group

was used to determine the number of easy discrimination sessions (three sessions of cumene versus 2-hexanone and two sessions for cyclohexanone versus isoamyl acetate) for the passive experience group.

Somatic functional imaging

For functional somatic imaging of abGCs and rGCs (Fig. 2), imaging was performed throughout the sessions of behavioral training or passive experience on D1, D3, D5, D7, and D9.

Dendritic structural imaging

For dendritic structural imaging of abGC and rGC dendrites (Fig. 3), structural z-stack was taken on D1, D3, D5, D7, and D9 before (typically, 2 hours) the sessions of task or passive experience.

Simultaneous functional and structural imaging of dendrites

For the simultaneous functional and structural imaging of abGC dendrites during task learning (Fig. 4), structural z-stack was taken on D1 and D9 before behavioral sessions, and functional imaging was done throughout the behavioral sessions on D3 and/or D7. For the structural imaging, odors were applied intermittently to visualize odor-responsive dendrites whose fluorescence was otherwise too dim to identify. Odor-suppressive dendrites (which are more active during the ITI) and nonresponsive dendrites (which usually show nonspecific spontaneous activity) were sufficiently bright to provide a good resolution for imaging the dynamics of spines (fig. S10). Attempts were made in the first imaging session to select similar numbers of odor-excitatory, odor-suppressive, and nonresponsive dendrites.

Optogenetic manipulation

Activation. Mice expressing ChrimsonR-tdTomato in the piriform cortex went through passive experience as described above for pretraining odors. At the stage with the passive experience of difficult-discrimination odorants, an LED light was delivered through the light pathway of a two-photon microscope to the glass window of the right olfactory bulb. The light was measured and adjusted to 10 mW before each experiment. The light onset and offset were controlled by the behavioral program to be on during the odor period (4 s) or the ITI period (fixed timing from 5.5 to 9.5 s from the beginning of the ITI). The LED (Thorlabs, M660L3) light was centered at 660 nm with a full width at half maximum of 10 nm. The LED was programmed using Arduino to 25 Hz with 10-ms pulses.

Inactivation. Mice expressing halorhodopsin-mCherry in the piriform cortex went through behavioral training as described above. At the 8-odor discrimination task stage, an LED light was delivered through an optical fiber (Doric Lenses, D204-2015-1.5) placed on top of the glass window of the right olfactory bulb. The light was measured and adjusted to 10 mW before each experiment. The light onset and offset were controlled by the behavioral program to be constantly on during the odor period (4 s). The LED (Doric Lenses, LEDC2_365/385) light was centered at 590 nm. The experimenters were blind to conditions of mice during the training and imaging.

Image acquisition

A commercial two-photon microscope (B-scope, Thorlabs) was used to perform in vivo imaging with 925-nm excitation (Mai Tai, Spectra-physics) at the frame rate of ~30 Hz. Each frame had a field of view of approximately 308 μm by 264 μm for the soma calcium imaging, approximately 142 μm by 121 μm for the piriform feedback imaging, and approximately 59 μm by 50 μm for the dendrite structural imaging with a resolution of 512 × 512 pixels. For functional imaging, each imaging segment consisted of 4000 consecutive frames (~134 s) and there was a 6-s intersegment interval between imaging segments. Trials during these intervals were excluded from the analysis. The imaging field was kept consistent across sessions by using the average image of the first imaging session as a template for the following sessions. For z-stack structural imaging (typically, ~30 μm in depth), a step size of 1 μm was used for GFP-labeled dendrites and 2 μm for GCaMP6s-labeled dendrites, and 100 frames of the image were taken at each step. Right after finishing the z-stack, motion correction and z-stack alignment were applied using custom MATLAB codes to obtain the max-projection image to ensure the image quality. Images of the landmarks around the dendrites were taken at lower zoom levels as the guide to locate the same dendrites in the subsequent sessions.

Data analysis and statistics

Calcium imaging

Time series images were saved as Tiff files and first processed for full-frame motion correction (55) and warping with custom MATLAB codes using the Triton Shared Computing Cluster (TSCC) provided by the University of California, San Diego (UCSD) supercomputer center.

Region of interests. After the motion correction, region of interests (ROIs) were drawn using a custom MATLAB GUI that was previously used in the laboratory (56). The ROIs were selected on the basis of the shape and size (~6- to 9-μm diameter) and should at least show fluorescent activity in one of the imaging sessions. For bouton imaging, one ROI was assigned to one bouton. For the first imaging session, ROIs corresponding to the cell bodies or boutons were manually drawn. The ROIs from the first session were transformed automatically to fit the imaging fields of subsequent sessions. Specifically, the initial ROI set from the first session was overlaid on the target imaging field, and a small portion of ROIs (usually five) from the initial ROI set were manually moved to the correct positions on the target image. These aligned ROIs were used as references to perform spatial transformation of the ROI set using a MATLAB built-in function *tformfwd*. After the automatic transformation, all ROIs were manually proofread to make sure they were in correct positions. For bouton imaging, the imaging fields with clear landmarks (for example, blood vessels, and two crossing or parallel long axons in the field) were chosen in the first session and used to go back to the same imaging field in the following sessions. ROIs were tracked on the basis of their relative positions to the landmarks. To estimate the fractions of axon-sharing boutons, we performed k-means clustering on the first imaging sessions. This approach identified 139 bouton clusters (that might belong to the same axons) in the task condition of 456 boutons (~30%) and 238 bouton clusters in the passive condition of 678 boutons (~35%).

For GC imaging, a surrounding area with relatively low fluorescence was chosen as the background ROI for each neuron. For bouton imaging, one background ROI was chosen for the whole imaging field because of the uniformly low background due to the sparse labeling.

The average pixel values of ROIs of the time series images were extracted by custom MATLAB codes using the TSCC. For all the ROIs, background fluctuations were adjusted in each frame by subtracting the difference between background ROI fluorescence of this frame and mean background ROI fluorescence of the imaging section (4000 frames) (57). The fluorescence time series data were aligned to trials on the basis of the behavior signals that were recorded concurrently.

Defining responsive odor-ROI pairs. Responsive odor-ROI pairs were defined as previously reported (*4*). An odor-ROI pair was classified as responsive if the following two criteria were met:

1) Within any sliding window of 0.5 s (~15 frames) during the odor delivery period, there are more than 75% of the image frames where the baseline (mean of baseline frames (the 5-s period before odor onset) of the trial) normalized F/F_0 of all trials are significantly different (Wilcoxon rank-sum test, $P < 0.01$) from baseline frames of all trials.

2) The average F/F_0 of all trials in at least one frame during the 0.5-s window (that meets criterion 1) is 0.20 (the cutoff threshold) larger (excitatory) or smaller (suppressive) than average baseline fluorescence of all trials.

We estimated the false-positive rate in our current dataset by applying the same criteria in the baseline activity (−4 to 0 s from odor onset) in the passive condition abGC recordings and found that the false-positive rate is 0.0031 for excitatory responses and 0.0035 for suppressive responses. We also examined the abGC mean activity of excitatory odor-ROI pairs and fraction of responsive odor-ROI pairs in the task condition with different cutoff thresholds [0.15 (less strict) and 0.25 (more strict)] and found the results to be similar (fig. S8, A to C).

The center of the time window that a given odor-ROI pair first reaches the criteria is considered as the onset latency of the odor-ROI pair. A small fraction of odor-ROI pairs exhibited both excitatory and suppressive responses on a given session. All of these ROI-odor pairs showed excitatory responses at the beginning of the odor period, followed by suppressive responses. We classified this response type as the onset-transient response.

Decoding

For each cell (or bouton) and each trial, the activity vector normalized to baseline (average of −5 to 0 s before odor onset) was obtained, and the mean of the baseline-normalized fluorescence during the odor period was used as the input. For each iteration, 7 cells and 47 trials were randomly selected for abGCs or rGCs (14 boutons for piriform feedback data) to train the support vector machine classifier. Before the training, the input vector of each cell was *z* scored. Fitcecoc function (MATLAB 2018a) was used to fit multiclass models (eight classes for eight odors) for support vector machine using the linear kernel function ["Learners" was defined as templateSVM ("KernelFunction," "linear") in MATLAB 2018a]. Ten-fold cross-validation was used to evaluate the classification error, and each dataset was repeated for 100 iterations. The mean decoding accuracy from all iterations was used as the final decoding accuracy.

Structural analysis

All scorers were blind to the identity of the dendrites. The structural dynamics of dendritic spines were quantified using a custom Python software. The software allows users to load images, adjust brightness and contrast, and manually annotate spines into different classes (new, stable, and eliminated). The software also provides the edge detection function that highlights the contour of spines and dendrites to assist manual annotation. All of the identified spines in the first session were categorized as "preexisting" spines. For the following sessions, spines were classified as either "new" or "stable" by the spine head and the spine root location compared with the previous session. After finishing the quantification for all sessions, the software computes spine numbers in each class (preexisting, stable, eliminated, and new). For each session, we confirmed that the previous session's stable spines + new spines = the current session's stable spines + "eliminated" spines. The correlation between the spine increase rate and the behavioral performance (mean correct rate of the last three sessions) was calculated using the standard machine learning package Scikit-learn in Python.

Whole-cell patch-clamp analysis. Peak, area, and mean amplitude of the response were calculated across the entire 1 s of optical stimulation, with a 1-s period immediately before light delivery used as baseline. Plateau voltage was estimated by taking the mean voltage across the last 200 ms of the light pulse train. Onset latency was calculated as the time from light pulse onset to the initial downward deflection of the excitatory postsynaptic current. Clampfit 11.1 was used for offline analyses.

Statistical analysis. All statistical analyses were performed in MATLAB or GraphPad (Prism 8). For two-sample comparisons, Welch's *t* test (for comparing samples with different standard deviations), *t* test, or paired *t* test was used for normally distributed data, otherwise Mann-Whitney's test or Wilcoxon signed-rank test was used. For multisample comparisons, one-way ANOVA (or repeated measures one-way ANOVA was used when the factor was repeated) or Kruskal-Wallis test (when data points were not normally distributed) was used. For comparisons between two time series, repeated measures two-way ANOVA was used. In the following cases, there were missing data due to human error or computer failures to save data, so mixed-effect analysis (Prism 8) was used instead of repeated measures two-way ANOVA: (i) Fig. 2F (for odor-pairs that were not odor-excitatory during certain sessions, the onset latency data were missing); (ii) Fig. 3F (right, newly added spines); (iii) Fig. 5D (two mice [one in the task group and one in the passive group] with incomplete data (imaging was only acquired until D5)]; and (iv) Fig. 6D: [two mice (one in the control group and one in the inactivation group) with incomplete data (training data of D9 were missing)]. Dunnett's test or Holm-Šídák's test was performed for post hoc multiple comparison with one-way ANOVA. Bonferroni-Šídák multiple comparison test was performed with two-way ANOVA. For one-way ANOVA, two-way ANOVA, and mixed-effect analysis, Greenhouse-Geisser correction was applied when sphericity assumption was not met. For the comparison of fractions between two samples, chi-square test was used.

REFERENCES AND NOTES

1. C. Blakemore, G. F. Cooper, Development of the brain depends on the visual environment. *Nature* **228**, 477–478 (1970).
2. G. M. Shepherd, W. R. Chen, C. A. Greer, in *The Synaptic Organization of the Brain*, G. M. Shepherd, Ed. (Oxford Univ. Press, 2004), pp. 165–216.
3. A. Wu, B. Yu, T. Komiyama, Plasticity in olfactory bulb circuits. *Curr. Opin. Neurobiol.* **64**, 17–23 (2020).
4. M. W. Chu, W. L. Li, T. Komiyama, Balancing the Robustness and Efficiency of Odor Representations during Learning. *Neuron* **92**, 174–186 (2016).
5. Y. Yamada, K. Bhaukaurally, T. J. Madarász, A. Pouget, I. Rodriguez, A. Carleton, Context- and output layer-dependent long-term ensemble plasticity in a sensory circuit. *Neuron* **93**, 1198–1212.e5 (2017).
6. A. Koldaeva, A. T. Schaefer, I. Fukunaga, Rapid task-dependent tuning of the mouse olfactory bulb. *eLife* **8**, e43558 (2019).

7. N. M. Abraham, V. Egger, D. R. Shimshek, R. Renden, I. Fukunaga, R. Sprengel, P. H. Seeburg, M. Klugmann, T. W. Margrie, A. T. Schaefer, T. Kuner, Synaptic inhibition in the olfactory bulb accelerates odor discrimination in mice. *Neuron* **65**, 399–411 (2010).

8. A. M. Boyd, J. F. Sturgill, C. Poo, J. S. Isaacson, Cortical feedback control of olfactory bulb circuits. *Neuron* **76**, 1161–1174 (2012).

9. A. M. Boyd, H. K. Kato, T. Komiyama, J. S. Isaacson, Broadcasting of cortical activity to the olfactory bulb. *Cell Rep.* **10**, 1032–1039 (2015).

10. G. H. Otazu, H. Chae, M. B. Davis, D. F. Albeanu, Cortical feedback decorrelates olfactory bulb output in awake mice. *Neuron* **86**, 1461–1477 (2015).

11. C. Lois, A. Alvarez-Buylla, Long-distance neuronal migration in the adult mammalian brain. *Science* **264**, 1145–1148 (1994).

12. P.-M. Lledo, M. Alonso, M. S. Grubb, Adult neurogenesis and functional plasticity in neuronal circuits. *Nat. Rev. Neurosci.* **7**, 179–193 (2006).

13. A. Mizrahi, Dendritic development and plasticity of adult-born neurons in the mouse olfactory bulb. *Nat. Neurosci.* **10**, 444–452 (2007).

14. L. Petreanu, A. Alvarez-Buylla, Maturation and death of adult-born olfactory bulb granule neurons: Role of Olfaction. *J. Neurosci.* **22**, 6106–6113 (2002).

15. K. A. Sailor, M. T. Valley, M. T. Wiechert, H. Riecke, G. J. Sun, W. Adams, J. C. Dennis, S. Sharafi, G.-L. Ming, H. Song, P.-M. Lledo, Persistent structural plasticity optimizes sensory information processing in the olfactory bulb. *Neuron* **91**, 384–396 (2016).

16. M. Alonso, C. Viollet, M.-M. Gabellec, V. Meas-Yedid, J.-C. Olivo-Marin, P.-M. Lledo, Olfactory discrimination learning increases the survival of adult-born neurons in the olfactory bulb. *J. Neurosci.* **26**, 10508–10513 (2006).

17. M. Lemasson, A. Saghatelyan, J.-C. Olivo-Marin, P.-M. Lledo, Neonatal and adult neurogenesis provide two distinct populations of newborn neurons to the mouse olfactory bulb. *J. Neurosci.* **25**, 6816–6825 (2005).

18. G. Lepousez, A. Nissant, A. K. Bryant, G. Gheusi, C. A. Greer, P.-M. Lledo, Olfactory learning promotes input-specific synaptic plasticity in adult-born neurons. *Proc. Natl. Acad. Sci. U.S.A.* **111**, 13984–13989 (2014).

19. A. Mouret, G. Gheusi, M.-M. Gabellec, F. de Chaumont, J.-C. Olivo-Marin, P.-M. Lledo, Learning and survival of newly generated neurons: When time matters. *J. Neurosci.* **28**, 11511–11516 (2008).

20. M. Yamaguchi, K. Mori, Critical period for sensory experience-dependent survival of newly generated granule cells in the adult mouse olfactory bulb. *Proc. Natl. Acad. Sci. U.S.A.* **102**, 9697–9702 (2005).

21. C. Rochefort, G. Gheusi, J.-D. Vincent, P.-M. Lledo, Enriched odor exposure increases the number of newborn neurons in the adult olfactory bulb and improves odor memory. *J. Neurosci.* **22**, 2679–2689 (2002).

22. J. L. Wallace, M. Wienisch, V. N. Murthy, Development and refinement of functional properties of adult-born neurons. *Neuron* **96**, 883–896.e7 (2017).

23. K. B. Quast, K. Ung, E. Froudarakis, L. Huang, I. Herman, A. P. Addison, J. Ortiz-Guzman, K. Cordiner, P. Saggau, A. S. Tolias, B. R. Arenkiel, Developmental broadening of inhibitory sensory maps. *Nat. Neurosci.* **20**, 189–199 (2016).

24. Y. Livneh, Y. Adam, A. Mizrahi, Odor processing by adult-born neurons. *Neuron* **81**, 1097–1110 (2014).

25. V. Breton-Provencher, M. Lemasson, M. R. Peralta III, A. Saghatelyan, Interneurons produced in adulthood are required for the normal functioning of the olfactory bulb network and for the execution of selected olfactory behaviors. *J. Neurosci.* **29**, 15245–15257 (2009).

26. F. Lazarini, M.-A. Mouthon, G. Gheusi, F. de Chaumont, J.-C. Olivo-Marin, S. Lamarque, D. N. Abrous, F. D. Boussin, P.-M. Lledo, Cellular and behavioral effects of cranial irradiation of the subventricular zone in adult mice. *PLOS ONE* **4**, e7017 (2009).

27. W. L. Li, M. W. Chu, A. Wu, Y. Suzuki, I. Imayoshi, T. Komiyama, Adult-born neurons facilitate olfactory bulb pattern separation during task engagement. *eLife* **7**, e33006 (2018).

28. M. Alonso, G. Lepousez, W. Sebastien, C. Bardy, M.-M. Gabellec, N. Torquet, P.-M. Lledo, Activation of adult-born neurons facilitates learning and memory. *Nat. Neurosci.* **15**, 897–904 (2012).

29. S. Bragado Alonso, J. K. Reinert, N. Marichal, S. Massalini, B. Berninger, T. Kuner, F. Calegari, An increase in neural stem cells and olfactory bulb adult neurogenesis improves discrimination of highly similar odorants. *EMBO J.* **38**, e98791 (2019).

30. J. Forest, L. Chalençon, M. Midroit, C. Terrier, I. Caillé, J. Sacquet, C. Benetollo, K. Martin, M. Richard, A. Didier, N. Mandairon, Role of adult-born versus preexisting neurons born at P0 in olfactory perception in a complex olfactory environment in mice. *Cereb. Cortex* **30**, 534–549 (2020).

31. W. Kelsch, C.-W. Lin, C. P. Mosley, C. Lois, A critical period for activity-dependent synaptic development during olfactory bulb adult neurogenesis. *J. Neurosci.* **29**, 11852–11858 (2009).

32. A. Nissant, C. Bardy, H. Katagiri, K. Murray, P.-M. Lledo, Adult neurogenesis promotes synaptic plasticity in the olfactory bulb. *Nat. Neurosci.* **12**, 728–730 (2009).

33. L. Vong, C. Ye, Z. Yang, B. Choi, S. Chua Jr., B. B. Lowell, Leptin action on GABAergic neurons prevents obesity and reduces inhibitory tone to POMC neurons. *Neuron* **71**, 142–154 (2011).

34. N. Mandairon, N. Kuczewski, F. Kermen, J. Forest, M. Midroit, M. Richard, M. Thevenet, J. Sacquet, C. Linster, A. Didier, Opposite regulation of inhibition by adult-born granule cells during implicit versus explicit olfactory learning. *eLife* **7**, e34976 (2018).

35. J.-C. Platel, A. Angelova, S. Bugeon, J. Wallace, T. Ganay, I. Chudotvorova, J.-C. Deloulme, C. Béclin, M.-C. Tiveron, N. Coré, V. N. Murthy, H. Cremer, Neuronal integration in the adult mouse olfactory bulb is a non-selective addition process. *eLife* **8**, e44830 (2019).

36. S. S. P. Magavi, B. D. Mitchell, O. Szentirmai, B. S. Carter, J. D. Macklis, Adult-born and preexisting olfactory granule neurons undergo distinct experience-dependent modifications of their olfactory responses In Vivo. *J. Neurosci.* **25**, 10729–10739 (2005).

37. A. Grelat, L. Benoit, S. Wagner, C. Moigneu, P.-M. Lledo, M. Alonso, Adult-born neurons boost odor–reward association. *Proc. Natl. Acad. Sci. U.S.A.* **115**, 2514–2519 (2018).

38. L. Huang, K. Ung, I. Garcia, K. B. Quast, K. Cordiner, P. Saggau, B. R. Arenkiel, Task learning promotes plasticity of interneuron connectivity maps in the olfactory bulb. *J. Neurosci.* **36**, 8856–8871 (2016).

39. M. T. Shipley, G. D. Adamek, The connections of the mouse olfactory bulb: A study using orthograde and retrograde transport of wheat germ agglutinin conjugated to horseradish peroxidase. *Brain Res. Bull.* **12**, 669–688 (1984).

40. R. Batista-Brito, J. Close, R. Machold, G. Fishell, The distinct temporal origins of olfactory bulb interneuron subtypes. *J. Neurosci.* **28**, 3966–3975 (2008).

41. W. Adams, J. N. Graham, X. Han, H. Riecke, Top-down inputs drive neuronal network rewiring and context-enhanced sensory processing in olfaction. *PLOS Comput. Biol.* **15**, e1006611 (2019).

42. M. E. Larkum, J. J. Zhu, B. Sakmann, A new cellular mechanism for coupling inputs arriving at different cortical layers. *Nature* **398**, 338–341 (1999).

43. H. Takahashi, J. C. Magee, Pathway interactions and synaptic plasticity in the dendritic tuft regions of CA1 pyramidal neurons. *Neuron* **62**, 102–111 (2009).

44. K. C. Bittner, C. Grienberger, S. P. Vaidya, A. D. Milstein, J. J. Macklin, J. Suh, S. Tonegawa, J. C. Magee, Conjunctive input processing drives feature selectivity in hippocampal CA1 neurons. *Nat. Neurosci.* **18**, 1133–1142 (2015).

45. K. C. Bittner, A. D. Milstein, C. Grienberger, S. Romani, J. C. Magee, Behavioral time scale synaptic plasticity underlies CA1 place fields. *Science* **357**, 1033–1036 (2017).

46. B. W. Strowbridge, Role of cortical feedback in regulating inhibitory microcircuits. *Ann. N. Y. Acad. Sci.* **1170**, 270–274 (2009).

47. R. T. Pressler, B. W. Strowbridge, Direct recording of dendrodendritic excitation in the olfactory bulb: Divergent properties of local and external glutamatergic inputs govern synaptic integration in granule cells. *J. Neurosci.* **37**, 11774–11788 (2017).

48. J. T. Gonçalves, S. T. Schafer, F. H. Gage, Adult Neurogenesis in the Hippocampus: From Stem Cells to Behavior. *Cell* **167**, 897–914 (2016).

49. M. S. Espósito, V. C. Piatti, D. A. Laplagne, N. A. Morgenstern, C. C. Ferrari, F. J. Pitossi, A. F. Schinder, Neuronal differentiation in the adult hippocampus recapitulates embryonic development. *J. Neurosci.* **25**, 10074–10086 (2005).

50. C. Schmidt-Hieber, P. Jonas, J. Bischofberger, Enhanced synaptic plasticity in newly generated granule cells of the adult hippocampus. *Nature* **429**, 184–187 (2004).

51. M. Bergami, G. Masserdotti, S. G. Temprana, E. Motori, T. M. Eriksson, J. Göbel, S. M. Yang, K.-K. Conzelmann, A. F. Schinder, M. Götz, B. Berninger, A critical period for experience-dependent remodeling of adult-born neuron connectivity. *Neuron* **85**, 710–717 (2015).

52. G. D. Clemenson, S. W. Lee, W. Deng, V. R. Barrera, K. S. Iwamoto, M. S. Fanselow, F. H. Gage, Enrichment rescues contextual discrimination deficit associated with immediate shock. *Hippocampus* **25**, 385–392 (2015).

53. C. D. Clelland, M. Choi, C. Romberg, G. D. Clemenson Jr., A. Fragniere, P. Tyers, S. Jessberger, L. M. Saksida, R. A. Barker, F. H. Gage, T. J. Bussey, A functional role for adult hippocampal neurogenesis in spatial pattern separation. *Science* **325**, 210–213 (2009).

54. A. Sahay, K. N. Scobie, A. S. Hill, C. M. O'Carroll, M. A. Kheirbek, N. S. Burghardt, A. A. Fenton, A. Dranovsky, R. Hen, Increasing adult hippocampal neurogenesis is sufficient to improve pattern separation. *Nature* **472**, 466–470 (2011).

55. A. Mitani, T. Komiyama, Real-time processing of two-photon calcium imaging data including lateral motion artifact correction. *Front. Neuroinform.* **12**, 98 (2018).

56. A. J. Peters, S. X. Chen, T. Komiyama, Emergence of reproducible spatiotemporal activity during motor learning. *Nature* **510**, 263–267 (2014).

57. H. K. Kato, M. W. Chu, J. S. Isaacson, T. Komiyama, Dynamic sensory representations in the olfactory bulb: Modulation by wakefulness and experience. *Neuron* **76**, 962–975 (2012).

Citation: A. Wu, B. Yu, Q. Chen, G. A. Matthews, C. Lu, E. Campbell, K. M. Tye, T. Komiyama, Context-dependent plasticity of adult-born neurons regulated by cortical feedback. *Sci. Adv.* **6**, eabc8319 (2020).

Science Advances

Context-dependent plasticity of adult-born neurons regulated by cortical feedback

An WuBin YuQiyu ChenGillian A. MatthewsChen LuEvan CampbellKay M. TyeTakaki Komiyama

View the article online
https://www.science.org/doi/10.1126/sciadv.abc8319
Permissions
https://www.science.org/help/reprints-and-permissions

Use of think article is subject to the Terms of service